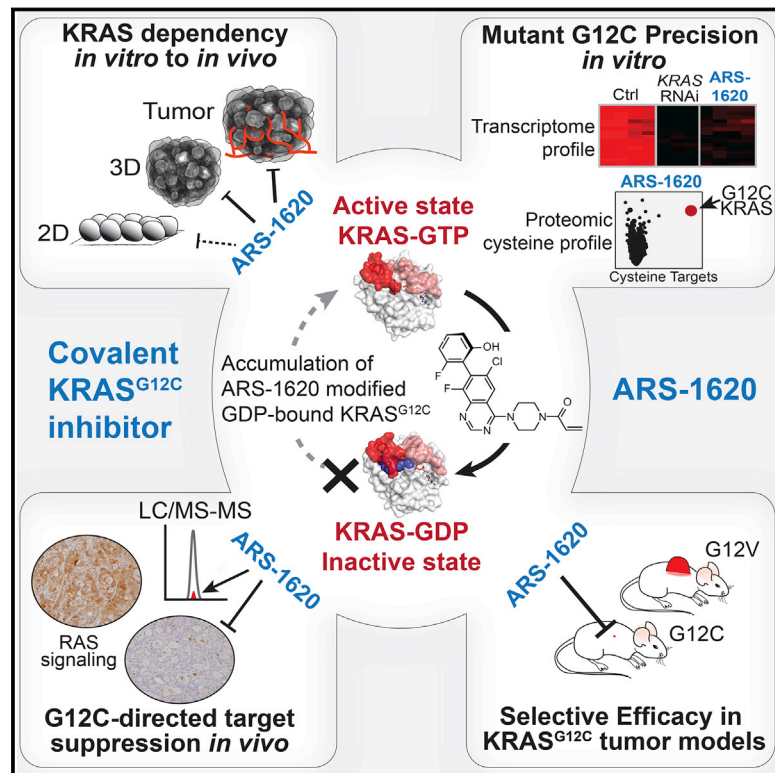Article

Targeting KRAS Mutant Cancers with a Covalent G12C-Specific Inhibitor

Graphical Abstract

Authors

Matthew R. Janes, Jingchuan Zhang,
Lian-Sheng Li, ..., Matthew P. Patricelli,
Pingda Ren, Yi Liu

Correspondence

yi@kuraoncology.com

In Brief

A covalent inhibitor specific for G12C mutant KRAS induces tumor regression in *in vivo* models.

Highlights

- ARS-1620, an atropisomeric selective KRAS[G12C] inhibitor with desirable PK

- ARS-1620 selectively induces tumor regression in patient-derived tumor models

- KRAS dependency is more profound *in vivo* compared to 2D-monolayer cell culture

- ARS-1620 is a valuable pharmacological tool to interrogate KRAS biology *in vivo*

CellPress

Targeting KRAS Mutant Cancers with a Covalent G12C-Specific Inhibitor

Matthew R. Janes,[1] Jingchuan Zhang,[1,5] Lian-Sheng Li,[1,5] Rasmus Hansen,[1] Ulf Peters,[1] Xin Guo,[1] Yuching Chen,[1] Anjali Babbar,[1] Sarah J. Firdaus,[1] Levan Darjania,[1] Jun Feng,[1] Jeffrey H. Chen,[1] Shuangwei Li,[1] Shisheng Li,[1] Yun O. Long,[1] Carol Thach,[1] Yuan Liu,[1] Ata Zarieh,[1] Tess Ely,[1] Jeff M. Kucharski,[1] Linda V. Kessler,[1] Tao Wu,[1] Ke Yu,[1] Yi Wang,[1] Yvonne Yao,[1] Xiaohu Deng,[1] Patrick P. Zarrinkar,[1] Dirk Brehmer,[2] Dashyant Dhanak,[3] Matthew V. Lorenzi,[3] Dana Hu-Lowe,[1] Matthew P. Patricelli,[1] Pingda Ren,[1,4] and Yi Liu[1,4,6,*]

[1]Wellspring Biosciences, San Diego, CA, USA
[2]Oncology Discovery, Janssen Research & Development, Beerse, Belgium
[3]Janssen Research & Development, Spring House, PA, USA
[4]Kura Oncology, San Diego, CA, USA
[5]These authors contributed equally
[6]Lead Contact
*Correspondence: yi@kuraoncology.com
https://doi.org/10.1016/j.cell.2018.01.006

SUMMARY

KRAS[G12C] was recently identified to be potentially druggable by allele-specific covalent targeting of Cys-12 in vicinity to an inducible allosteric switch II pocket (S-IIP). Success of this approach requires active cycling of KRAS[G12C] between its active-GTP and inactive-GDP conformations as accessibility of the S-IIP is restricted only to the GDP-bound state. This strategy proved feasible for inhibiting mutant KRAS *in vitro*; however, it is uncertain whether this approach would translate to *in vivo*. Here, we describe structure-based design and identification of ARS-1620, a covalent compound with high potency and selectivity for KRAS[G12C]. ARS-1620 achieves rapid and sustained *in vivo* target occupancy to induce tumor regression. We use ARS-1620 to dissect oncogenic KRAS dependency and demonstrate that monolayer culture formats significantly underestimate KRAS dependency *in vivo*. This study provides *in vivo* evidence that mutant KRAS can be selectively targeted and reveals ARS-1620 as representing a new generation of KRAS[G12C]-specific inhibitors with promising therapeutic potential.

INTRODUCTION

KRAS mutations have wide-spread prevalence in human cancers (Bos, 1989). The missense mutation of *KRAS* at codon 12 aberrantly activates the protein into a hyperexcitable state by attenuating its GTPase activity resulting in accretion of GTP-bound activated KRAS (Lito et al., 2016; Patricelli et al., 2016; Pylayeva-Gupta et al., 2011) and activation of downstream signaling pathways (Downward, 2003). *KRAS p.G12C* mutations predominate in NSCLC comprising 11%–16% of lung adenocar-cinomas (45%–50% of mutant *KRAS* is *p.G12C*) (Campbell et al., 2016; Jordan et al., 2017), as well as 1%–4% of pancreatic and colorectal adenocarcinomas, respectively (Bailey et al., 2016; Giannakis et al., 2016).

Despite this prevalence, mutant KRAS has remained an intractable therapeutic target despite decades of extensive effort (Cox et al., 2014). A variety of virtual, high-throughput, and fragment-based screening strategies have been attempted to identify small molecules that target KRAS. Strategies pursued include disruption of active state conformations of switch-I (aa 30–38) and switch-II (aa 59–76) regions that facilitate guanine nucleotide exchange factor (GEF) interaction (Burns et al., 2014; Evelyn et al., 2014; Leshchiner et al., 2015; Maurer et al., 2012; Patgiri et al., 2011; Sun et al., 2012) and effector binding (Shima et al., 2013; Welsch et al., 2017), or targeting the nucleotide-binding site (Lim et al., 2014; Xiong et al., 2016) and adjacent shallow surface pockets, which include the recently discovered allosteric pocket under the switch II loop region (S-IIP) (Ostrem et al., 2013) also summarized in Ostrem and Shokat (2016).

While many of these innovative approaches demonstrated previously unknown binding pockets on RAS, they had resulted in only limited demonstration of sufficient target suppression of KRAS in cells and all critically lack demonstration of *in vivo* responses with convincing proof of on-target mechanism of action. Because of the lack of a pharmacological tool to inhibit KRAS *in vivo*, the community is left with engineered systems and RNAi targeted approaches to interrogate KRAS addiction and mutant KRAS dependency *in vivo*. These challenges combined with the clinically unmet need for a viable therapy to target KRAS motivated our structure-based drug design to improve potency and drug-like properties of mutant-directed and KRAS-specific inhibitors.

We and others have previously described a series of S-IIP G12C KRAS inhibitors that bind to and covalently react with the GDP-bound state of KRAS[G12C] trapping it in an inactive conformation (Lito et al., 2016; Patricelli et al., 2016). Using ARS-853 (and analogs), both groups reported profound depletion of KRAS-GTP that corresponded to covalent occupancy of Cys-12 of KRAS[G12C] in cells, along with downstream RAS

signaling inhibition. Together, the two reports provided evidence that KRAS[G12C] does cycle its nucleotide state in cells, such that targeting its inactive GDP-bound state could sequester KRAS and exhaust the active conformation. A critically unanswered question remained from these studies to pave a path toward therapeutic potential—will it work *in vivo*?

There is a large uncertainty whether this approach will work *in vivo* due to the inherent mechanistic restriction of targeting the S-IIP that is solely accessible in the GDP-bound inactive state. Although we previously reported rapid cycling of the KRAS nucleotide-bound state in cells can permit near-complete KRAS engagement under constant exposure of a KRAS[G12C] inhibitor in cell culture, it is unknown if the extent of engagement *in vivo* under a finite exposure window of a covalent inhibitor can capture enough KRAS-GDP from cycling to its GTP active conformation. To approach this question, there are two major obstacles. First, the inhibitor must have high potency and rapid binding kinetics to allosterically capture the GDP-bound inactive state of KRAS[G12C] undergoing a rapid nucleotide cycle. The second obstacle is to optimize pharmacokinetics (PK) properties to maintain a sufficient exposure and duration to drive near-complete covalent target engagement of the GDP-bound state. To do so, a KRAS[G12C] inhibitor needs to exhibit a favorable balance of ADME attributes, *in vivo* stability, and target reactivity, such that non-specific reactivity to promiscuous nucleophiles (plasma proteins) commonly encountered in blood are minimized (Strelow, 2017). Although this ideal PK scenario poses a challenge for all covalent inhibitors with reactive warheads, the S-IIP targeted approach will require the exposure of the inhibitor to be maintained above a threshold concentration for sufficient duration to maximize capture of the GDP-state cycled from the GTP-bound majority *in vivo*. Whether it is feasible to overcome these challenges for *in vivo* proof of concept is currently unknown.

Here, we report the design and characterization of a class of S-IIP G12C inhibitors with improved potency and pharmacologic properties that overcome limitations of the initial ARS-853 series. We describe a compound ARS-1620, with features necessary to achieve sufficient *in vivo* covalent target occupancy to inhibit KRAS-GTP in tumors. We provide proof of concept and mechanistic support for the covalent and mutant allele-specific precision of ARS-1620 across *p.G12C KRAS* mutant cell lines and *in vivo* tumor models. This effort validates mutant KRAS as a central oncogenic driver in KRAS[G12C] mutant tumor models, provides support for targeting the S-IIP of KRAS as a viable therapeutic strategy for *p.G12C KRAS* mutant cancers, and represents a major step toward bringing KRAS inhibitors to the clinic.

RESULTS

Designing Switch-II Pocket KRAS[G12C] Inhibitors with Improved Potency and Drug-like Properties

Major chemistry challenges exist for optimizing potency and pharmacologic properties of previously reported S-IIP KRAS[G12C] inhibitors. To illustrate this, we synthesized numerous analogs within the ARS-853 series and summarize their biochemical/cellular target activity with specific pharmacologic features. Using liquid chromatography-tandem mass spectrom-

etry (LC/MS-MS)-based assays (Patricelli et al., 2016) that directly and quantitatively measure compound covalent adduct formation at Cys-12 of KRAS, we report the most potent compound (ARS-853) modifies KRAS with average biochemical and cellular rate constants (k_{obs}/[I]) of 140–150 $M^{-1}s^{-1}$. A major drawback of the series is short metabolic stability in plasma ($t_{1/2} < 20$ min) and poor oral bioavailability in mice (F < 2%) making it unfeasible for further *in vivo* exploration (Figure 1A).

Narrow structure activity relationships (SAR) have restricted the ARS-853 series from further potency improvement. Furthermore, the *ortho*-amino phenol moiety and glycine linker within the core scaffold of the series are metabolic hotspots and sources of poor plasma stability and ADME/PK liabilities (Stepan et al., 2011). We therefore shifted our focus to design structurally distinct scaffolds that appropriately position the conformation and trajectory of the acrylamide warhead and allow optimum distance for proper placement of the hydrophobic binding moiety within the S-IIP. We hypothesized that the flexible 2-amino-1-(piperazin-1-yl)ethan-1-one linker of the ARS-853 series could be shortened and replaced with a more rigid bicyclic scaffold and fit into the unoccupied region between S-II and α3 helix as revealed by our previously reported ARS-853 co-crystal structure (Patricelli et al., 2016). Following extensive scaffold optimization, we identified a quinazoline core as a versatile lead scaffold that could overcome the SAR restrictions of ARS-853 and possess better drug-like properties (Figure 1B). This advancement led to a quinazoline-based series (Li et al., 2015) and resulted in a substantial improvement in KRAS covalent binding activity with favorable ADME/PK potential following systematic optimization of substituents around the scaffold (Figure 1C).

ARS-1620 Covalently Inhibits KRAS[G12C] Activity with High Potency and Atropisomeric Selectivity in p.G12C Mutant Cancer Cells

Several compounds with improved activity were synthesized from the quinazoline series. Among the top hits was a compound, ARS-1620, which contains a fluorophenol hydrophobic binding moiety with axial chirality rendering atropisomeric reactivity of the *S*-atropisomer for the Cys-12 of KRAS (Figure 2A). The co-crystal structure of ARS-1620 bound to KRAS[G12C] reveals a distinct binding mode and trajectory from initial S-IIP KRAS[G12C] inhibitors to reach Cys-12 and reveals acquisition of an additional and key interaction with His-95 leading to a more rigidified and favorable conformation for covalent reaction than compounds in the ARS-853 series (Figures 2B–2D; Table S1). The improvement in potency of ARS-1620 from prior compounds for modifying KRAS was demonstrated in biochemical assays where ARS-1620 covalently modifies KRAS[G12C] with an observed rate of 1,100 ± 200 $M^{-1}s^{-1}$ (k_{obs}/[I]), a 10-fold improvement over ARS-853. The *R*-conformational atropisomer is nearly 1,000-fold less potent than ARS-1620 (1.2 ± 0.6 $M^{-1}s^{-1}$) and thus serves as a unique inactive control compound (Figure 2E). The stereodynamics of the two atropisomers are conformationally stable and lack any detectable interconversion (see the STAR Methods). The remarkable selectivity between the atropisomers is structurally explained by the conformational orientation of the fluorophenol moiety where the hydroxyl group on the active *S*-atropisomer (ARS-1620) occupies a solvated region
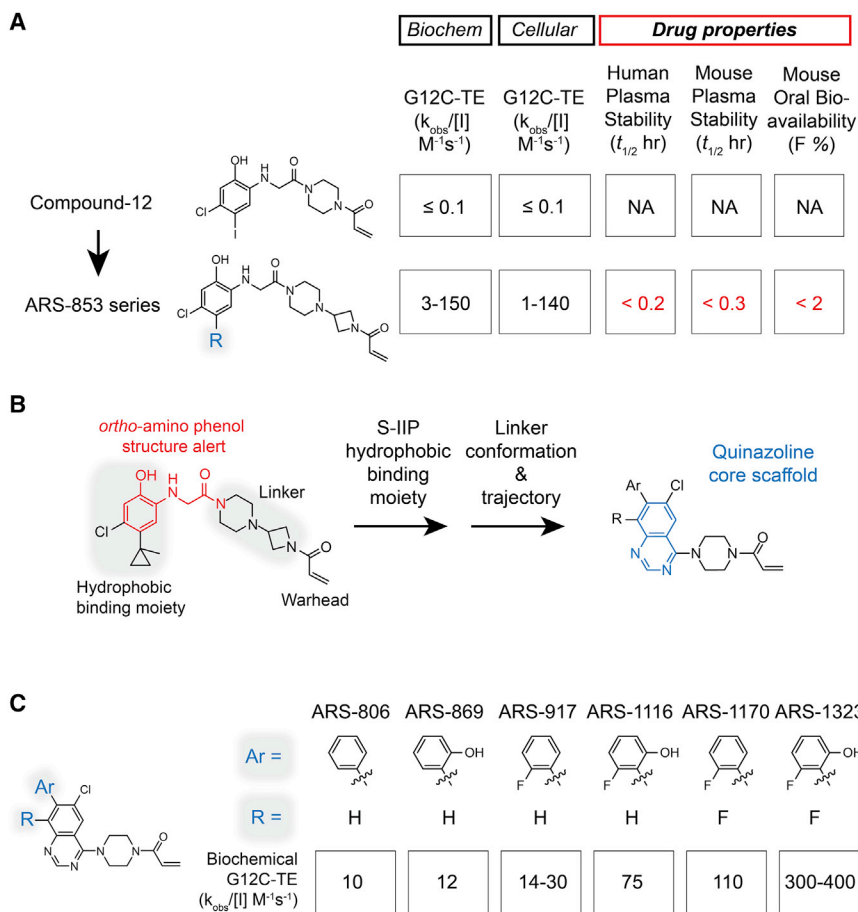
Figure 1. Optimization of Potency and Drug Properties of Existing S-IIP KRAS[G12C] Inhibitors

(A) Summary of biochemical and cellular rate constants for KRAS[G12C] covalent target engagement (G12C-TE) and drug properties of existing compounds.

(B) Identification of a quinazoline core scaffold that improves potency and drug properties of S-IIP KRAS[G12C] inhibitors.

(C) SAR summary of biochemical rate constants of G12C-TE associated with substituents at the 7- and 8-position of the quinazoline core. Reported rate constants of compounds with chiral substituents were tested as racemic mixtures.

baseline GDP/GTP-bound KRAS[G12C] and nucleotide cycling rates (Figure S2).

To determine the effect of KRAS-specific inhibition on RAS pathway activation, we assessed H358 (*p.G12C*) and negative control lung cancer cells lacking *p.G12C* (A549, H460, and H441) following a 24-hr treatment period with ARS-1620, the inactive *R*-atropisomer, and a saturated acrylamide analog of ARS-1620, which is unable to form a covalent bond with cysteine. Consistent with G12C target engagement results, ARS-1620 inhibited RAS-GTP (RAF-RBD pull-down affinity), and the phosphorylation of MEK, ERK, RSK, S6, and AKT in a dose-dependent and selective manner in H358 but not in negative control cell lines (Figure 3B). In contrast, the inactive *R*-atropisomer and saturated (non-covalent) analogs lacked any observable effects on RAS signaling at all tested compound concentrations (≥ 10 μM). We next compared the activity of ARS-1620 to ARS-853 for inhibiting RAS signaling and found ARS-1620 exhibited >10× potency improvement (120 nM IC$_{50}$ versus 1,700 nM IC$_{50}$), consistent with G12C occupancy, and yields a >100-fold window of mutant allele selectivity in cells (Figures 3 and S3A).

We next monitored the kinetics of RAS pathway inhibition over both acute (between 0.5 to 6 hr) and long-term time courses (up to 48 hr) of treatment. The effects of ARS-1620 on RAS signaling closely matched G12C target engagement and was consistent with inhibiting both RAS-GTP and KRAS-GTP (using either a pan-RAS isoform or a KRAS-isoform selective antibody, respectively) following RBD pull-down. This observation is consistent with specificity for KRAS[G12C] and supported by LC/MS-MS-based evidence (Patricelli et al., 2016) that mutant KRAS is the predominating (>95%) GTP-active isoform in RBD pull-down fractions from *p.G12C* mutant cancer cells (Figures S3B–S3D). The durability of RAS-GTP suppression was maintained for treatment periods as long as 48 hr (Figure S3E). This is further supported by G1 cell-cycle arrest (Figures S3F–S3H) and significantly increased apoptosis induction (Figures S3F, S3I, and S3J) in *p.G12C* mutant cells treated with ARS-1620.

and forms multiple water-mediated hydrogen bonds to KRAS residues while the fluoro group occupies a hydrophobic region (Figure 2C). Consistent with other S-IIP KRAS[G12C] inhibitors mode of action (Ostrem et al., 2013; Patricelli et al., 2016), ARS-1620 preferentially engages the GDP nucleotide-bound state of KRAS[G12C] and lacks detectable reactivity on any residue of wild-type (WT)-KRAS protein (Figure 2E). Furthermore, KRAS[G12C] covalently bound to ARS-1620 lacks SOS- and EDTA-mediated nucleotide exchange capacity consistent with a previously reported trapping mechanism of KRAS[G12C] into a GDP-bound inactive state (Figures 2F and S1) (Lito et al., 2016; Ostrem et al., 2013; Patricelli et al., 2016).

We next assessed the potency and kinetics of ARS-1620 covalent modification of KRAS[G12C] across a panel of cell lines (n = 4) harboring the mutant allele. ARS-1620 rapidly engaged G12C in a concentration- and time- dependent manner consistent with its covalent mechanism of inhibition (Figure 3A). After 2 hr of treatment, ARS-1620 exhibited a half maximal G12C target engagement (TE$_{50}$) at ~0.3 μM and near complete engagement at 3.0 μM. In comparison, the *R*-atropisomer lacked any relevant target occupancy. Cellular engagement kinetics of ARS-1620 closely matched previously reported global-fit modeling parameters (Patricelli et al., 2016) that described the observed engagement rates of ARS-853 in the context of a kinetic model that incorporates experimentally determined
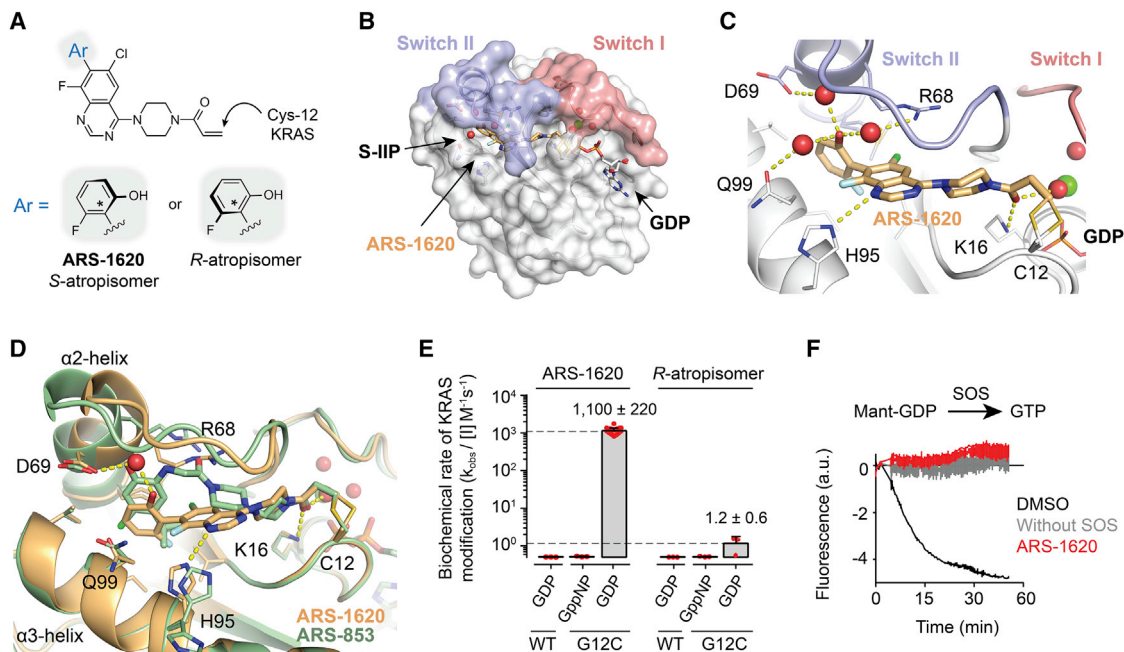
Figure 2. Basic Characterization of ARS-1620, an Allele-Specific Covalent Inhibitor of GDP-Bound Mutant KRAS^{G12C}

(A) Chemical structure of ARS-1620. The aryl (Ar) hydrophobic binding moiety is a site of axial chirality and atropisomerism (gray boxes).

(B) ARS-1620 (gold) and GDP-bound KRAS^{G12C} co-crystal structure (PDB: 5V9U) with locations of switch 1 (blue), switch 2 (pink), and induced switch 2 pocket (S-IIP) regions. See also Table S1.

(C) Binding mode of ARS-1620 and KRAS^{G12C} from co-crystal structure.

(D) Comparison of binding modes and key interactions of ARS-1620 (gold) and ARS-853 (green).

(E) Biochemical covalent modification and preference of the S-atropisomer (ARS-1620) for GDP-loaded recombinant KRAS^{G12C} protein over GppNP-loaded mutant or WT KRAS. Biochemical rate constants (k_{obs}/[I], M^{-1}s^{-1}, mean ± SD, n = ≥3) for KRAS modification of each atropisomer (10 μM) is shown.

(F) SOS-mediated nucleotide exchange release assay with mant-GDP bound KRAS^{G12C} protein pre-labeled with ARS-1620, and unlabeled GTP as excess incoming nucleotide.

See also Figure S1.

To assess the effects on inhibiting cell growth, we profiled ARS-1620, the R-atropisomer, and saturated analogs across a panel of cancer cell lines harboring either *KRAS p.G12C* (H358, MIA-PaCa2, and LU65), or other mutant *KRAS* alleles (H441, A549, and HCT116) over a 5-day treatment period. ARS-1620 exhibited complete growth suppression of *p.G12C* cell lines (150 nM IC$_{50}$) with relatively benign effects on control cell lines. Additionally, the R-atropisomer and saturated analogs lacked any significant effect on growth suppression up to 10 μM of compound concentration (Figure 3C). Moreover, the inhibitory effects of ARS-1620 could be rescued with inducible overexpression of KRAS^{G12V} (Figures 3D and S3K) and were selective to KRAS^{G12C} ectopically expressing Ras-less MEFs but not WT, G12D, or G12V *KRAS* alleles (Figure 3E). Together, these data demonstrate ARS-1620 elicits sub-micromolar allele-specific potency (IC$_{50}$ ≤0.3 μM; IC$_{90}$ ≤1 μM) and strongly supports the activity of ARS-1620 is specific to the G12C allele and mediated by the covalent modification of Cys-12.

Targeting an Oncogenic Driver with Mutant Allele-Specific Precision

A primary risk for covalent inhibitors is the potential for non-specific reactivity with off-target proteins. There are ~200

kinases with reactive cysteines near the ATP pocket (Liu et al., 2013), and likewise extends to non-kinase proteins with reactive cysteines (Strelow, 2017) that if targeted could produce an unwanted idiosyncratic toxicity. To better define possible off-target liabilities and specificity of ARS-1620, we assessed the intracellular covalent reactivity using an unbiased chemical proteomic screen with resolution covering 8,501 cysteine residues across 3,012 annotated proteins. Following a 4-hr treatment period with ARS-1620, we identified Cys-12 of KRAS as the most substantially and significantly engaged cysteine in the proteome (p = 1.15 × 10^{-5}) (Figure 4A). This is consistent with kinetic results targeting the Cys-12 tryptic peptide of G12C and near saturation of occupancy (Figures 3A and S2) and covers concentrations and time required to inhibit downstream RAS signaling inhibition (Figures 3B and S3) in previous experiments. ARS-1620 also modified cysteines of FAM213A and AHR that are commonly observed targets of covalent compounds (including clinically approved) that employ acrylamide warheads (Lanning et al., 2014). To further understand the potential off-target liabilities of ARS-1620, we profiled the cysteine selectivity of the R-atropisomer devoid of KRAS Cys-12 reactivity and found that both rotamers exhibit similar reactivity toward FAM213A and AHR (Figure 4B). These data corroborate the Cys-12 allele-specific KRAS target profile
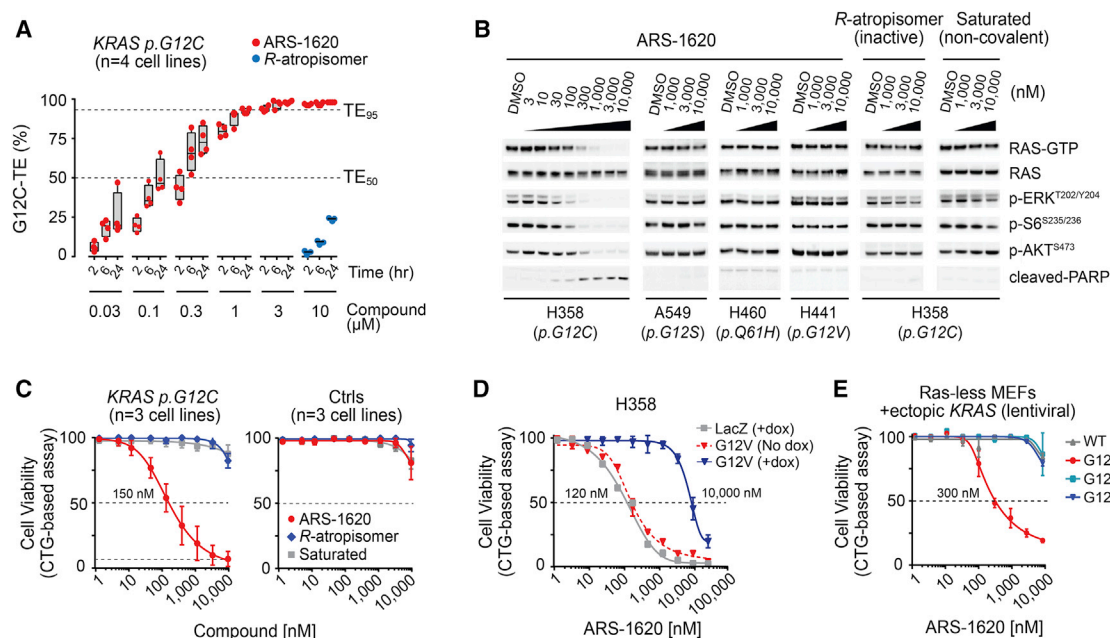
Figure 3. Validation of ARS-1620 Allele-Specific Inhibition of KRAS[G12C] in Cells

(A) Time course and dose response of ARS-1620 and *R*-atropisomer cellular engagement of KRAS[G12C] (G12C-TE). Presented as median ± interquartile range (IQR) across *KRAS p.G12C* cell lines (n = 4, with 3 technical replicates per data point). Dotted lines represent concentrations necessary to achieve half maximal (TE$_{50}$) or 95% (TE$_{95}$) G12C target engagement. See also Figure S2.

(B) RAS-GTP pull-down and immunoblot analysis of KRAS mutant lung cancer cells following a 24 hr treatment with DMSO or ARS-1620, *R*-atropisomer, or an analog of ARS-1620 containing a saturated acrylamide.

(C) The anti-proliferative effects of ARS-1620 analogs on *KRAS p.G12C* mutant cell lines (n = 3) or control cell lines lacking G12C (n = 3) following 5 days of treatment.

(D) Rescue of ARS-1620 anti-proliferative effects in H358 cells by inducible overexpression of FLAG-KRAS[G12V] (n = 2 technical replicates).

(E) The anti-proliferative effect of ARS-1620 on Ras-less MEFs ectopically expressing human WT, G12C, G12D, or G12V KRAS (n = 2 technical replicates). See also Figure S3.

of ARS-1620 and supports parallel use of the *R*-atropisomer as a unique chemical control to rule out possible off-target activities in downstream assessments.

We next employed a transcriptome profiling strategy to elucidate components of the oncogenic KRAS network and expose any associated gene transcription relationships that would relate to the functional selectivity of ARS-1620. To approach this, we compared genome-wide gene expression profiles of ARS-1620- or DMSO-treated H358 cells and H358 cells stably expressing either a pLKO.1 luciferase control or a *KRAS* small hairpin RNA (shRNA) (knockdown [KD]). Clustering analysis revealed a similarity between ARS-1620-treated and *KRAS* shRNA-expressing-KD cells (KRAS-KD). 4,988 genes were differentially expressed both in ARS-1620-treated and KRAS-KD cells, as compared to their respective controls (Figure 4C). Three distinct clusters of differentially regulated genes were observed. The largest cluster with significant downregulation composed a KRAS-regulated network enriched of genes linked to transformation by oncogenic *KRAS* (Barbie et al., 2009; Chiaradonna et al., 2006; Liberzon et al., 2015), such as E2F transcription factors (Liberzon et al., 2015), a MYC regulatory network (Bild et al., 2006), ERK activation (Dry et al., 2010; Kwong et al., 2015), and KRAS-dependency signatures (Singh et al., 2009; Sweet-Cordero et al., 2005; Vallejo et al., 2017) from curated *in vitro* exper-

imental systems silencing KRAS and tumor types that classify patients by KRAS genotype (Figures 4D, S4A, and S4B; Table S2).

To further investigate RAS pathway-regulated genes, we extended our comparison to the expression profiles of H358 and LU65 (*p.G12C*) versus non-G12C KRAS mutant cells (A549) following treatment with ARS-1620. 2,820 genes were differentially expressed and overlapped with *KRAS* knockdown, trametinib-, and ARS-1620-treated cells, with 185 genes overlapping with the greatest significance (>2 absolute log$_2$ fold change, false discovery rate [FDR] q < 0.01) (Figures S4C and S4D; Table S3). Using a curated KRAS-dependency gene set (23 genes) we found ARS-1620 significantly reduced expression of the gene set in *p.G12C* mutant cells in a time-dependent manner but not in the *p.G12S* mutant cells (Figures S4D–S4F). Among the ARS-1620 regulated genes that were significantly unique to ARS-1620 and not modulated by KRAS-KD cells, were those involved in xenobiotic metabolism, CYP induction (e.g., P450 enzymes), and redox oxidation/reduction-type processes (Figures 4C, 4D, and S4G) and are likely associated with the cellular pharmacology of the covalent inhibitor. Collectively, these gene expression relationships build a molecular correlate and further support for ARS-1620 working through inhibiting an oncogenic network downstream of KRAS[G12C].
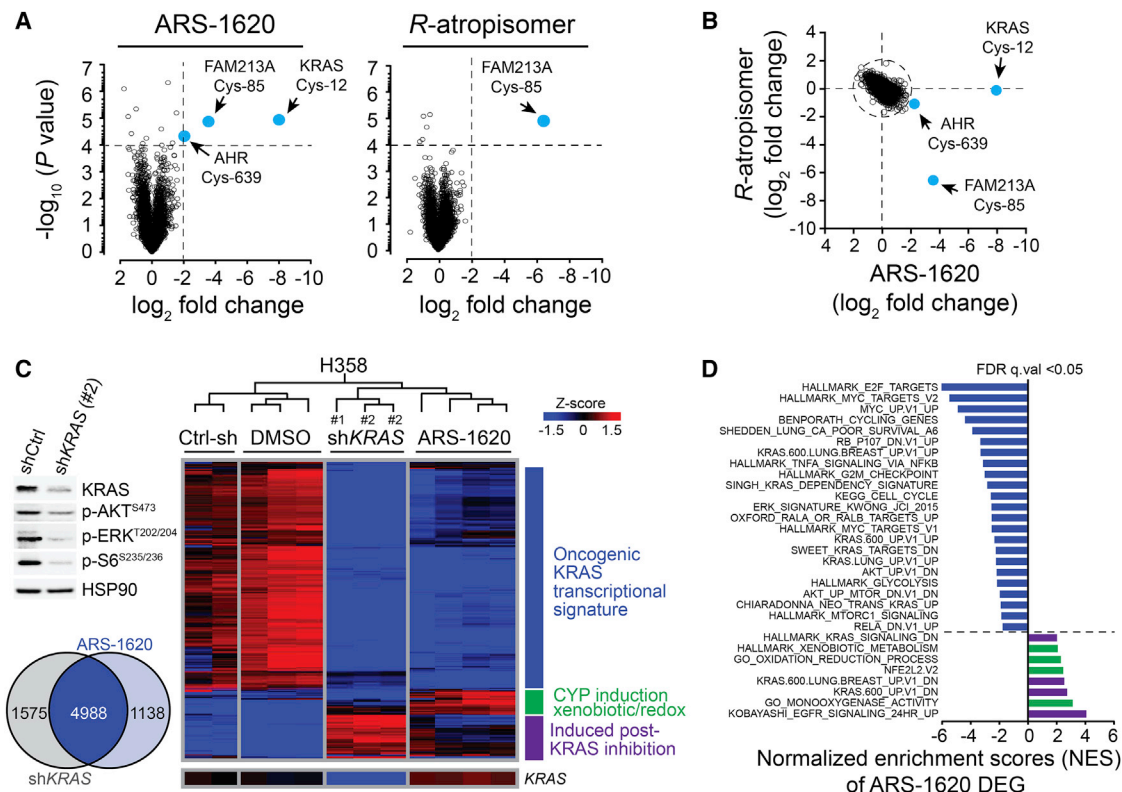
Figure 4. Proteome and Transcriptome Profiling the Functional Selectivity of ARS-1620 for KRAS^{G12C} and Associated Gene Transcription Signatures

(A) Cysteines targeted for covalent modification across the proteome of H358 cells following a 4-hr treatment with ARS-1620 (4 μM) or the *R*-atropisomer (4 μM). Criteria for covalent targets (blue dots) is >2 log$_2$ fold change with p value less than 1×10^{-4} across biologic replicates (n = 3).

(B) Comparison of peptides containing cysteines modified by ARS-1620 and the *R*-atropisomer following a 4-hr treatment (4 μM).

(C) Hierarchical clustering of top 300 differentially regulated genes (FDR <0.05) following transduction (48 hr post) with shRNAs to *KRAS* (using 2 unique shRNAs), *luc* (as Ctrl-sh), or treatment (24 hr post) with ARS-1620 (1 μM) or DMSO. 2–4 independent biologic replicates per group. KRAS knockdown was confirmed by immunoblotting (left) and *KRAS* gene expression is magnified at the bottom of the heatmap. Venn diagram (bottom left) illustrates overlap of differentially expressed genes (DEG) with FDR <0.05.

(D) GSEA of transcriptional changes significantly enriched (FDR <0.05) following ARS-1620 treatment.

See also Figure S4.

ARS-1620 Induces Tumor Regression through an On-Target Mechanism of Action

Developing a therapeutic to block RAS activity with sufficient pharmacologic properties has proven difficult to accomplish. Through structure-based design optimization of the quinazoline scaffold, we were able to sufficiently achieve reasonable drug-like properties while maintaining potency and covalent kinetics in cells (Figure 5A). ARS-1620 exhibits excellent oral bioavailability (F > 60%) in mice and sufficient blood stability essential for quantitative measurements of *in vivo* G12C target occupancy. Although rapid engagement of G12C is achieved in cells despite the GDP-bound nucleotide state preference of the chemical series, it is still unknown whether sufficient covalent kinetic and pharmacokinetic properties can be met for a S-IIP G12C targeting approach to succeed *in vivo*. To address if ARS-1620 has the capacity to elicit *in vivo* target occupancy, we orally administered ARS-1620 in established subcutaneous xenograft models bearing *KRAS p.G12C*. Following a single oral dose or 5 consecutive daily doses, ARS-1620 yielded

average peak tumor concentrations of 1.5 μM (50 mg/kg) and 5.5 μM (200 mg/kg), respectively, that enabled significant KRAS^{G12C} target occupancy (≥70% G12C-TE at 200 mg/kg) for >24 hr (Figures 5B and S5A). At these exposures, ARS-1620 elicited a dose- and time-dependent inhibition of RAS-GTP that tracked with covalent G12C modification in xenografts of MIA-PaCa2 and H358 following a single dose (Figures 5C, S5B, and S5C). The target coverage also extended to a 3-day consecutive daily dose schedule of ARS-1620 (200 mg/kg), providing significant G12C target occupancy (75% to 90% G12C-TE) as well as RAS-GTP and downstream signaling inhibition (Figure 5D).

We next addressed if the target occupancy achieved can translate to *in vivo* anti-tumor activity. To demonstrate this, we orally administered ARS-1620 in established subcutaneous xenograft models bearing *KRAS p.G12C* or *p.G12V*. In MIA-PaCa2 xenografts (*p.G12C*), ARS-1620 significantly inhibited tumor growth (p < 0.001) in a dose-dependent manner with marked regression at a dose of 200 mg/kg, given once daily (Figure 5E,
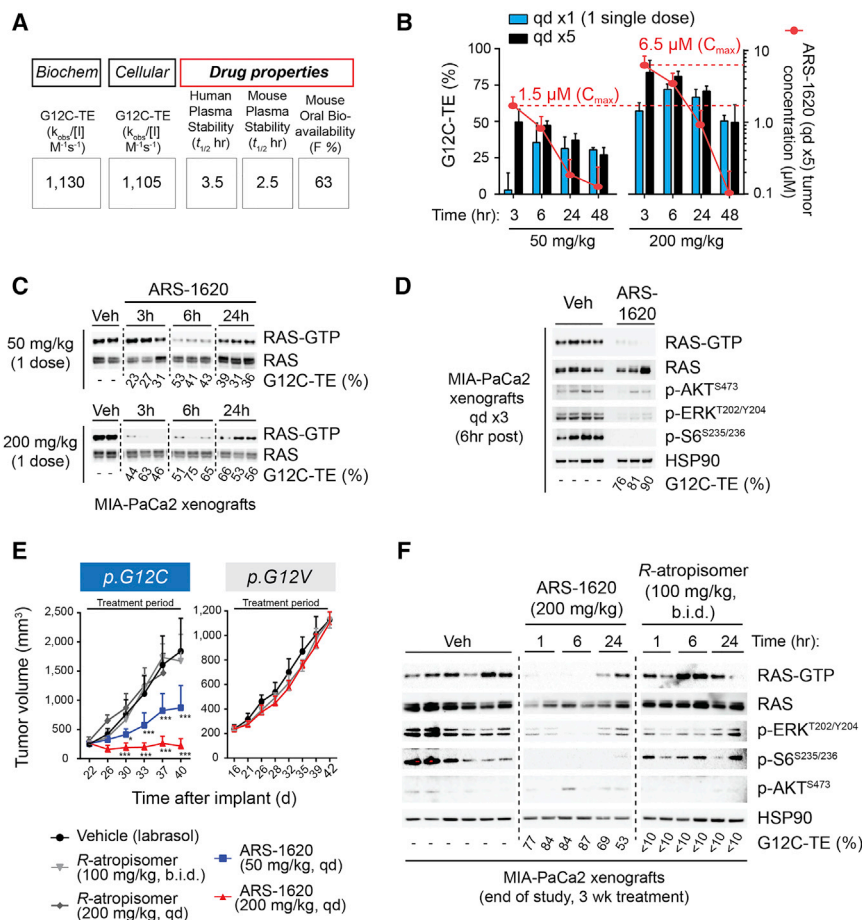
Figure 5. ARS-1620 Exhibits Favorable Pharmacologic Properties and Therapeutic Efficacy in a Mutant Allele-Specific Manner

(A) Summary of biochemical, cellular G12C-TE, and drug properties of ARS-1620.

(B) Pharmacodynamics (PD)/PK assessment of G12C-TE and exposure of ARS-1620 (μM) in tumors following single (qd ×1) or five consecutive days (every day [qd] ×5) oral administration to MIA-PaCa2 xenografts (n = 4 per group).

(C) RAS-GTP levels by RBD pull-down affinity complemented by LC/MS-MS analysis of G12C-TE in tumor lysates following a single dose of vehicle or ARS-1620.

(D) RAS signaling inhibition and G12C-TE following 3 consecutive daily doses of vehicle or ARS-1620 (200 mg/kg, 6 hr after last dose).

(E) Anti-tumor efficacy of ARS-1620 or the *R*-atropisomer in subcutaneous MIA-PaCa2 (*p.G12C*) or H441 (*p.G12V*) xenografts (n = 8 mice per group, mean ± SD), *p < 0.05, ***p < 0.001.

(F) G12C-TE and effects on RAS activity in tumors following 3 weeks of daily treatment.

See also Figure S5.

KRAS mutant models including those harboring *p.G12C*. If only a minority of *KRAS* mutant cancers actually depend on KRAS as an oncogenic driver, this would have profound impact on the therapeutic feasibility of a G12C targeted strategy. We therefore approached this systematically and assembled a panel of *KRAS p.G12C* cancer cell lines (n = 15) and compared their KRAS dependency relationships from *in vitro* culture systems to *in vivo* tumor xenograft models using ARS-1620 as a pharmacological tool.

We directly compared monolayer (2D-adherent) and 3D ultra-low adherent (ULA) suspension spheroid cultures in our *in vitro* screen to rule out the possibility of cell adherence attenuating sensitivity to ARS-1620—similar to reports of culture adherence affecting KRAS mutant cells to *KRAS* knockdown (Fujita-Sato et al., 2015; Patricelli et al., 2016; Vartanian et al., 2013). Following a 5-day treatment period, only a minority of G12C mutant cell lines were sensitive to ARS-1620 under monolayer culture conditions (Figure 6A, top panel), whereas in 3D-spheroid conditions, ARS-1620 elicited a robust response (p = 0.0140) (Figure 6A, bottom panel). Across both culture settings, non-G12C cell lines lacked any significant effect up to 10 μM of compound concentration. Comparing the KRAS-dependence sensitivity scores (ATARiS) from the Project DRIVE RNAi screen (McDonald et al., 2017) provided moderately accurate association to ARS-1620 sensitivity as 2D-adherent monolayers, a format used for the Project DRIVE screen. Together, these data corroborate inherent differences in KRAS dependence in different culture systems.

To establish the *in vivo* relevance to this observation, we next asked whether ARS-1620 would elicit *in vivo* responses that track with the variable sensitivity observed *in vitro*. To approach

left panel). Xenografts of H441 (*p.G12V*) lacked a response at all doses tested (Figure 5E, right panel) and the *R*-atropisomer of ARS-1620 lacked activity in both models, demonstrating the specificity of the response. Following 3 weeks of treatment, G12C target occupancy of ARS-1620 in tumors was sufficient to elicit profound RAS-GTP and downstream signaling inhibition. Consistent with *in vitro* observations, the *R*-atropisomer exhibited negligible G12C target occupancy and lacked effects on RAS pathway activation (Figures 5F and S5D).

Systematic Evaluation of KRAS Dependency Reveals Differential Sensitivity to KRAS Inhibition between *In Vitro* and *In Vivo* Tumor Models
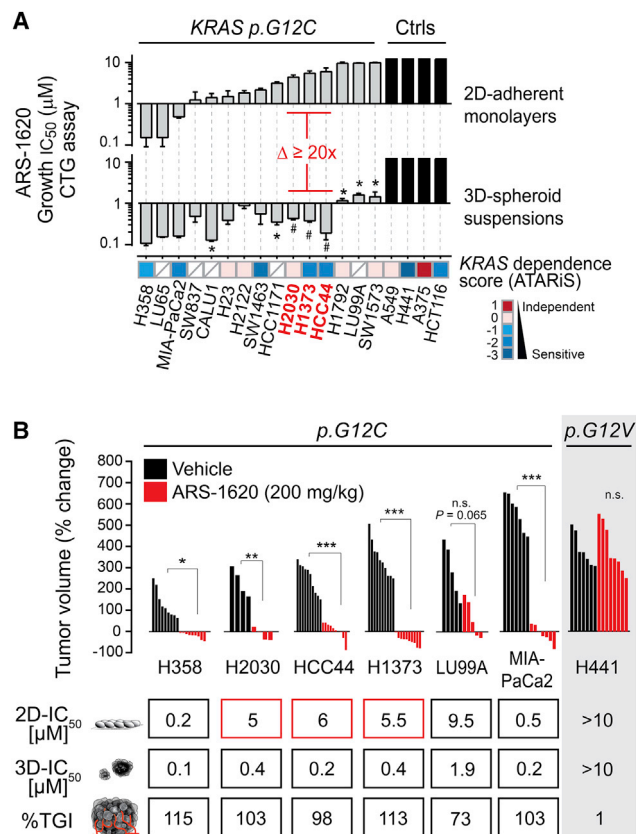
Following establishment that ARS-1620 elicits *in vivo* anti-tumor activity with allele-specific precision, we next sought to investigate how broadly dependent *p.G12C* cancer models are for mutant KRAS. Numerous reports have observed heterogeneous dependence for sustained *KRAS* expression (<50% addicted) across KRAS mutant cancer cell lines (Hayes et al., 2016; Kapoor et al., 2014; Lamba et al., 2014; Patricelli et al., 2016; Shao et al., 2014; Singh et al., 2009; Sunaga et al., 2011; Vartanian et al., 2013), for example, a large-scale RNAi screen known as Project DRIVE (McDonald et al., 2017) reports KRAS independence following shRNA knock down of *KRAS* in commonly used

Figure 6. Comprehensive Anti-tumor Response across *p.G12C* Tumor Models Reveals Translational Implications for Assessing KRAS Dependence *In Vitro*

(A) ARS-1620 growth IC_{50} across *p.G12C* cell lines (n = 15) as 2D-adherent monolayers or ultra-low adherent (ULA) 3D-spheroid suspensions following 5 days of treatment (mean ± SD, n ≥ 3 independent experiments). #≥20-fold (colored red) or *5-fold increased sensitivity in 3D. KRAS dependence scores (ATARiS) from Project DRIVE are displayed as a heatmap, where checked squares represent no data available.

(B) Percent change in tumor volume following 2–3 weeks of treatment across 7 different *KRAS* mutant (n = 6 *p.G12C* and n = 1 *p.G12V*) cell line xenograft models. n = 4–10 mice per group, *p < 0.05, **p < 0.01, ***p < 0.001. Bottom panel depicts *in vitro* growth IC_{50} values in 2D or 3D formats and average percent tumor growth inhibition (TGI). Red boxes accentuate the models with refractory response in 2D.

this question, we profiled the response of NSCLC cell line xenograft models (n = 5), of which 4 of 5 are predicted to be completely refractory to treatment based on 2D growth response, whereas from 3D, the *in vivo* responses are anticipated to be sensitive (Figure 6A). Following a 2- to 3-week treatment period, all 5 NSCLC models responded (>70% tumor growth inhibition [TGI]) with 4 out of 5 models exhibiting significant tumor growth suppression (p < 0.01) and marked tumor regression in >50% of animals (Figure 6B). Noteworthy is the response of H2030, H1373, and HCC44 xenografts, as the *in vitro* response as 3D-spheroids is >20× the response as monolayers (~0.3 μM 3D-IC_{50} versus ~5.5 μM 2D-IC_{50}). These findings strengthen support that 3D-spheroid systems best predict the magnitude of an *in vivo* anti-tumor response from

KRAS[G12C]-directed therapies. These results also imply a sense of caution for deducing *in vivo* KRAS addiction from *in vitro* monolayer culture systems.

ARS-1620 Displays Potent and Selective Anti-tumor Activity in PDX Tumor Models

To further demonstrate therapeutic efficacy with ARS-1620, we profiled anti-tumor responses in a panel of patient-derived (PDX) tumor xenograft models harboring *KRAS p.G12C* (n = 4) compared to PDX models that lack the mutant allele (n = 3) (also see Table S4 for targeted sequencing results). The *p.G12C* PDX panel comprised three adenocarcinoma NSCLCs, which is a potential target indication with the greatest frequency of *KRAS p.G12C* mutations (11%–16%) in patients (Campbell et al., 2016; Jordan et al., 2017) and a pancreatic adenocarcinoma that represents a minor proportion (<2%) of KRAS mutant pancreatic cancers (Bailey et al., 2016).

ARS-1620 induced significant TGI (p < 0.001) and marked regression in *p.G12C* PDX models following 3 weeks of treatment using a daily 200 mg/kg schedule, whereas non-G12C bearing xenografts lacked any response (Figure 7A). We confirmed on average ≥75% G12C target occupancy of ARS-1620 in tumors at the end of study (6 hr post last dose) using a daily 200 mg/kg treatment schedule (Figure 7B). Additionally, ARS-1620 significantly inhibited p-ERK and p-S6 across the *p.G12C* PDX models (p < 0.05) (Figures 7C, S6A, and S6B). This resulted in significant apoptosis induction (p = 0.0148) as monitored by immunohistochemistry (IHC) staining of cleaved caspase-3 (Figure 7D). We next assessed if ARS-1620 administered at higher doses or frequency could improve the target occupancy and efficacy in tumor-bearing animals. Both 200 mg/kg twice daily (b.i.d.) or 400 mg/kg once daily schedules of ARS-1620 provided improved response rates in *p.G12C* PDX models (Figure 7A) and were associated with stronger p-ERK inhibition (Figures S6A–S6C), consistent with greater G12C occupancy as observed in cell-line-derived xenograft models (Figures S5E–S5H). Across all tumor models employed, ARS-1620 was well tolerated over the entire 3-week treatment period (Figures S6D and S6E). Moreover, there were no observed clinical signs or toxicity of ARS-1620 in CD-1 mice even at oral doses up to 1,000 mg/kg administered daily over a 7-day period (see Animal Studies in the STAR Methods). Above 400 mg/kg, ARS-1620 exhibits PK saturation and hence no further enhancement of anti-tumor efficacy was achieved in cell line-derived and PDX-derived models (data not shown). In summary, ARS-1620 is generally well-tolerated and the maximum tolerated dose (MTD) was not reached in mice. Collectively, the *in vivo* efficacy and mutant selectivity observations of ARS-1620 across a variety of KRAS[G12C] mouse cancer models support future therapeutic strategies for covalently targeting the S-IIP of KRAS.

DISCUSSION

Despite decades of research highlighting mutant *KRAS* as a central driver of tumorigenesis and clinical resistance, the development of therapeutics directly targeting mutant KRAS has so far been unaccomplished. The lack of clear druggable pockets on KRAS sufficiently large enough for small molecule binding
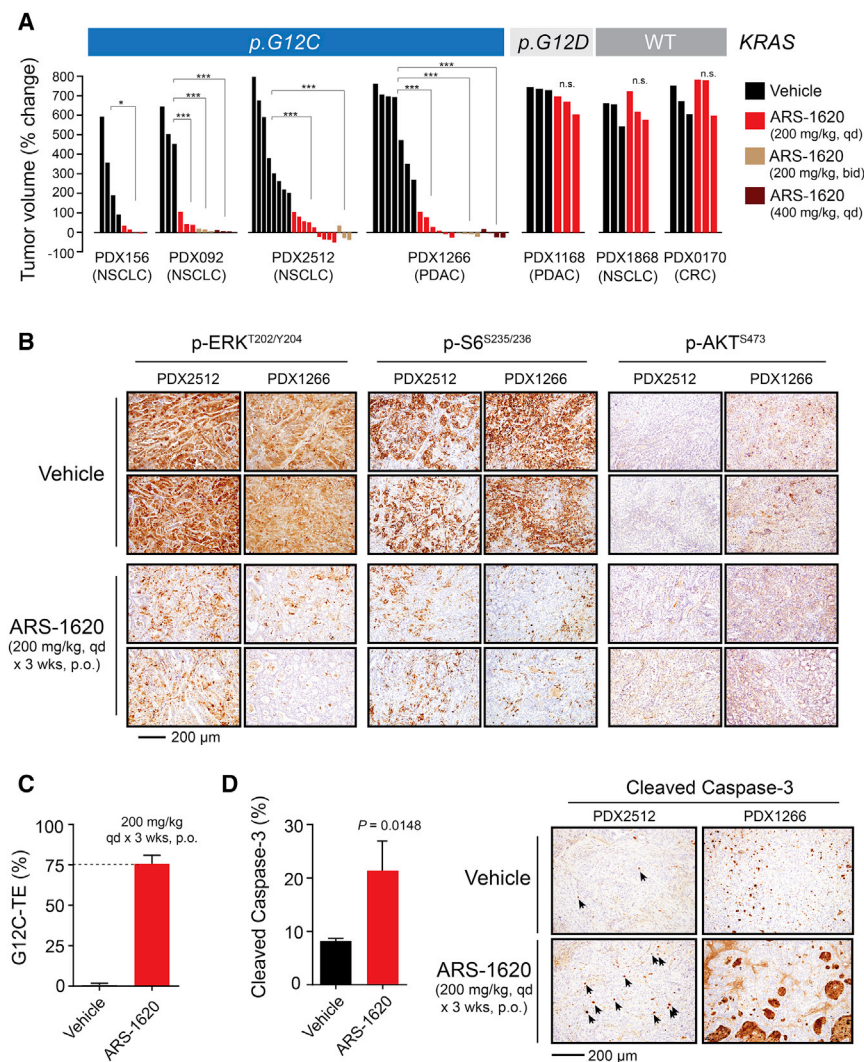
Figure 7. Validating ARS-1620 Efficacy in Patient-Derived Tumor Xenograft Models

(A) Percent change in tumor volume following 3 weeks of treatment of established patient-derived tumor xenografts (PDX) harboring *KRAS p.G12C* (n = 4), *p.G12D* (n = 1, PDX1168), or WT alleles, whereas PDX1868 harbors $EGFR^{T790M;L858R}$ driver mutations, and PDX0170 harbors Lynch syndrome mutations in *PMS2*, *MSH2*, *MSH6*, and *APC*. See Table S4 for targeted sequencing at baseline. Treatment schedules consisted of vehicle or ARS-1620 (200 mg/kg, qd, or b.i.d; or 400 mg/kg, qd; n = 3–9 per group), *p < 0.05, ***p < 0.001.

(B) IHC assessment of p-ERK, p-S6, and p-AKT from representative *p.G12C* PDX tumors following 3 weeks of treatment (1 hr after last dose).

(C) G12C-TE (mean ± SD) from *p.G12C* tumors (PDX156, PDX2512, PDX1266) following 3 weeks of treatment (n = 3–6 per model).

(D) IHC assessment of cleaved caspase-3 in *p.G12C* models (PDX2512, PDX1266; n = 6 per group) following 3 weeks of treatment (1 hr after last dose), mean ± SD.

See also Figure S6.

ity to preclude an on-target and RAS-directed mechanism of action. In contrast, the S-IIP class of covalent $KRAS^{G12C}$ inhibitors (Lito et al., 2016; Ostrem et al., 2013; Patricelli et al., 2016), despite their initial lack of potency, can produce very specific and demonstrably targeted effects on the mutant allele in cells. The most advanced inhibitor in the series, ARS-853, has improved potency in the low micro-molar range in cells (Patricelli et al., 2016), but the inherent poor chemical and metabolic stability of this series has made it unsuitable for use in animal models (see Figure 1A).

imposes extensive challenges for therapeutic targeting. Shallow pockets and fragment-based ligands have been identified on KRAS (Maurer et al., 2012; Ostrem et al., 2013) other than the nucleotide-binding site but none have led to identification of inhibitors with suitable potency. Currently, all reported small molecule binders to KRAS are biochemically weak and display micromolar activity necessitating substantial improvement for therapeutic use. It is therefore a major chemistry challenge to improve the potency of a direct KRAS inhibitor, especially within a pocket with highly dynamic and induced-fit conformational changes such as the S-IIP.

Among the reported classes of small molecule KRAS binders, few have confirmed an on-target molecular mechanism of action in both biochemical and cellular settings. Although recent reports of small molecule binders to RAS isoforms have described activity in both *in vitro* and *in vivo* models (Athuluri-Divakar et al., 2016; Welsch et al., 2017), large discrepancies exist between the concentrations necessary for biochemical binding to RAS (high micro-molar) and those needed to elicit cellular and *in vivo* activ-

As a result of the lack of pharmacological tools to evaluate anti-tumor activity of directly targeting mutant KRAS *in vivo*, it remains unknown whether directly targeting KRAS with a small molecule inhibitor is therapeutically effective and feasible. To address the major challenge that exists for the S-IIP-targeted strategy to work *in vivo*, significant hurdles had to be overcome: the rate of covalent engagement to G12C must be sufficient to access the GDP-bound state in rapid cycle within a tumor, and the inhibitor must balance this optimal potency and selectivity with a favorable PK profile.

This report describes ARS-1620 as the first example of a direct $KRAS^{G12C}$ small molecule inhibitor that is potent, selective, orally bioavailable, and well-tolerated for comprehensive and in-depth investigation of $KRAS^{G12C}$ *in vitro* and *in vivo*. Despite mechanistic specificity for bonding the GDP-bound form of mutant KRAS, ARS-1620 maintains sufficient PK to engage G12C *in vivo* following a single oral dose—trapping the mutant in an inactive state. This finding, therefore, extends our *in vitro* observations of rapid nucleotide cycling of $KRAS^{G12C}$ to *in vivo* human cancer

cell line- and patient-derived tumor models. In retrospect, achieving a combination of high covalent potency and sufficiently high and durable exposure to trap the GDP-bound state has been the largest hurdle to accomplish for drug design of the S-IIP targeted strategy, which has comprised hundreds of synthesized candidates. Despite this challenge, it is fortuitous to note that the PK profile and covalent rate of bond formation *in vivo* for ARS-1620 enables ≥75% target occupancy for an extended period of time at the doses employed, and the data show this degree of occupancy is necessary and sufficient to achieve therapeutic efficacy in tumor models. We envisage strategies that maximize G12C target occupancy *in vivo* will be an important property to wield while moving forward into clinical development for this class of compounds. Another therapeutic consideration we must consider emerges from the result that KRAS^{G12C} cycles nucleotides *in vivo*; whereby, it may be possible to boost compound engagement with G12C through rational targeted combinations with upstream RTK inhibitors (e.g., EGFR) that facilitate accessibility of the GDP-bound state of KRAS^{G12C} by shifting the cellular KRAS bound GDP/GTP ratio in favor of KRAS^{G12C}-GDP, as demonstrated *in vitro* with ARS-853 (Lito et al., 2016; Patricelli et al., 2016). Innovative treatment schedules that take advantage of the covalent and irreversible mechanism may also reveal strategies that maximize G12C occupancy for the greatest therapeutic effect for this targeted approach. Given the high on-target selectivity of KRAS^{G12C} inhibitors for the mutant allele, we anticipate this to translate to less side effects and higher tolerability *in vivo*. Indeed, ARS-1620 is well-tolerated in mice as the MTD has not been reached. Collectively, ARS-1620 represents a novel class of direct KRAS inhibitors with *in vitro* to *in vivo* potency and therapeutic window in the range of a drug candidate.

The strength and breadth of KRAS dependency across KRAS mutant cancers *in vivo* has remained underexplored due to the lack of a pharmacological tool. RNAi-based approaches have yielded numerous accounts of variable sensitivity to *KRAS* silencing using KRAS mutant cancer cell lines and large-scale shRNA screens (Hayes et al., 2016; Lamba et al., 2014; McDonald et al., 2017; Singh et al., 2009; Sunaga et al., 2011; Vartanian et al., 2013). Differential sensitivity to continued expression of mutant *KRAS* has also been affirmed when examined under adherent monolayer versus 3D culture settings (Fujita-Sato et al., 2015; Patricelli et al., 2016; Vartanian et al., 2013). In this report, we investigated KRAS dependency in the setting of *KRAS p.G12C* cancer cell lines. Utilizing ARS-1620 as a pharmacologic tool, this study systematically demonstrates the correlation of oncogenic KRAS dependency between *in vitro* systems and *in vivo* NSCLC tumor models. We incorporated in our study G12C mutant cancer cells with a range of sensitivity to KRAS depletion confirmed by a meta-analysis from the Project DRIVE sensitivity network (McDonald et al., 2017). Using this cell line panel, we confirmed differential sensitivity to KRAS inhibition *in vitro* with ARS-1620 in cell lines with both low and high KRAS dependency scores and also confirmed culture-dependent effects of KRAS dependency across monolayer versus 3D-spheroids. We now can extend these KRAS-dependency relationships to the *in vivo* setting. The finding that ARS-1620 is highly efficacious as a single agent in multiple cell

line- and patient-derived mouse xenograft models highlights the central importance of mutant KRAS driving cancer growth and survival *in vivo*. Moreover, our findings not only imply that 3D-spheroid cultures better predict the *in vivo* sensitivity of KRAS mutant cancer cells to ARS-1620, they lend support that *in vitro* studies assessing KRAS dependency using adherent monolayer cell cultures significantly underestimate KRAS dependence *in vivo*. This has dramatic translational implications for interpreting *in vitro* synthetic lethal relationships of *KRAS* as a driving oncogene. Although 3D cultures are becoming more frequently appreciated and utilized to better mimic the *in vivo* environment and response to chemotherapy (Selby et al., 2017) and other therapeutic targets (e.g., HER2 and EGFR) (Ekert et al., 2014; Howes et al., 2014; Pickl and Ries, 2009; Weigelt et al., 2010), we are not aware of any approved oncology drugs that display differential activity between 2D and 3D cultures as substantial as KRAS inhibition. The patient response rate in future clinical trials to a KRAS^{G12C}-directed drug will be an excellent test of the value of using 3D cultures to predict clinical response to therapeutics.

Collectively, the *in vivo* evidence that ARS-1620 is broadly efficacious as a single agent across NSCLC models provides proof of concept that a significant portion of patients with *p.G12C KRAS* mutations may benefit from KRAS^{G12C}-directed therapies. Our study provides the first *in vivo* evidence that the S-IIP targeted approach may be a promising therapeutic strategy for patients with *KRAS p.G12C* mutant cancers.

STAR★METHODS

Detailed methods are provided in the online version of this paper and include the following:

- KEY RESOURCES TABLE
- CONTACT FOR REAGENT AND RESOURCE SHARING
- EXPERIMENTAL MODEL AND SUBJECT DETAILS
  - Cell lines and bacterial strains
  - Animal studies
  - Pharmacokinetic (PK) studies in mice
  - Cell line and patient-derived xenograft studies in mice
  - Toxicity assessment in mice
- METHOD DETAILS
  - Chemistry and synthesis of chemical materials
  - Atropisomer interconversion
  - Plasmids, lentiviral production, and recombinant proteins
  - Crystallization, data collection, and refinement
  - KRAS biochemical modification
  - Nucleotide exchange assay
  - Plasma stability
  - Cell proliferation assays
  - Cell cycle and apoptosis assays
  - Lentivirus mediated shRNA knockdown
  - Immunoblotting and RAS-GTP pulldown
  - Cysteine selectivity profiling
  - Cellular KRAS^{G12C} target engagement (G12C-TE)
  - Tumor KRAS^{G12C} target engagement (G12C-TE)
  - Immunohistochemistry (IHC)

- ○ Transcriptome sequencing, library preparation, and gene set analysis
- ○ Targeted sequencing and library preparation
- QUANTIFICATION AND STATISTICAL ANALYSIS
- DATA AND SOFTWARE AVAILABILITY

AUTHOR CONTRIBUTIONS

M.R.J. and Yi Liu wrote the paper. L.-S.L. led as project leader, designed, and supervised chemistry. M.R.J., L.-S.L., J.Z., M.P.P., P.R., and Yi Liu conceived, designed, and supervised the overall project. M.R.J. designed, analyzed, and supervised in vitro experiments, tumor PD and IHC assessment, and bioinformatics. J.Z. designed, analyzed, and supervised in vivo experiments. L.D. supervised pharmacology experiments. R.H. conceived and designed mass spectrometry experiments. U.P. conceived and designed in vitro biochemical experiments and crystallography. D.H.-L. and P.P.Z. managed and supervised the project and edited the paper. Y.C., A.B., J.H.C., S.J.F., J.M.K., L.V.K., T.E., and D.B. performed in vitro experiments. X.G., Shuangwei Li, and C.T. performed in vivo experiments. Shisheng Li, K.Y., A.Z., Y.W., and Y.Y. performed PK-related experiments. J.F., Y.O.L., Yuan Liu, T.W., and X.D. performed chemistry synthesis. D.B., D.D., and M.V.L. helped facilitate conceptualization, overall project progression, and revise the paper.

REFERENCES

Athuluri-Divakar, S.K., Vasquez-Del Carpio, R., Dutta, K., Baker, S.J., Cosenza, S.C., Basu, I., Gupta, Y.K., Reddy, M.V., Ueno, L., Hart, J.R., et al. (2016). A small molecule RAS-mimetic disrupts RAS association with effector proteins to block signaling. Cell *165*, 643–655.

Bailey, P., Chang, D.K., Nones, K., Johns, A.L., Patch, A.M., Gingras, M.C., Miller, D.K., Christ, A.N., Bruxner, T.J., Quinn, M.C., et al.; Australian Pancreatic Cancer Genome Initiative (2016). Genomic analyses identify molecular subtypes of pancreatic cancer. Nature *531*, 47–52.

Barbie, D.A., Tamayo, P., Boehm, J.S., Kim, S.Y., Moody, S.E., Dunn, I.F., Schinzel, A.C., Sandy, P., Meylan, E., Scholl, C., et al. (2009). Systematic RNA interference reveals that oncogenic KRAS-driven cancers require TBK1. Nature *462*, 108–112.

Bild, A.H., Yao, G., Chang, J.T., Wang, Q., Potti, A., Chasse, D., Joshi, M.B., Harpole, D., Lancaster, J.M., Berchuck, A., et al. (2006). Oncogenic pathway signatures in human cancers as a guide to targeted therapies. Nature *439*, 353–357.

Bos, J.L. (1989). ras oncogenes in human cancer: a review. Cancer Res. *49*, 4682–4689.

Burns, M.C., Sun, Q., Daniels, R.N., Camper, D., Kennedy, J.P., Phan, J., Olejniczak, E.T., Lee, T., Waterson, A.G., Rossanese, O.W., and Fesik, S.W. (2014). Approach for targeting Ras with small molecules that activate SOS-mediated nucleotide exchange. Proc. Natl. Acad. Sci. USA *111*, 3401–3406.

Campbell, J.D., Alexandrov, A., Kim, J., Wala, J., Berger, A.H., Pedamallu, C.S., Shukla, S.A., Guo, G., Brooks, A.N., Murray, B.A., et al.; Cancer Genome Atlas Research Network (2016). Distinct patterns of somatic genome alterations in lung adenocarcinomas and squamous cell carcinomas. Nat. Genet. *48*, 607–616.

Chen, V.B., Arendall, W.B., 3rd, Headd, J.J., Keedy, D.A., Immormino, R.M., Kapral, G.J., Murray, L.W., Richardson, J.S., and Richardson, D.C. (2010). MolProbity: all-atom structure validation for macromolecular crystallography. Acta Crystallogr. D Biol. Crystallogr. *66*, 12–21.

Chiaradonna, F., Sacco, E., Manzoni, R., Giorgio, M., Vanoni, M., and Alberghina, L. (2006). Ras-dependent carbon metabolism and transformation in mouse fibroblasts. Oncogene *25*, 5391–5404.

Cox, A.D., Fesik, S.W., Kimmelman, A.C., Luo, J., and Der, C.J. (2014). Drugging the undruggable RAS: Mission possible? Nat. Rev. Drug Discov. *13*, 828–851.

Downward, J. (2003). Targeting RAS signalling pathways in cancer therapy. Nat. Rev. Cancer *3*, 11–22.

Dry, J.R., Pavey, S., Pratilas, C.A., Harbron, C., Runswick, S., Hodgson, D., Chresta, C., McCormack, R., Byrne, N., Cockerill, M., et al. (2010). Transcriptional pathway signatures predict MEK addiction and response to selumetinib (AZD6244). Cancer Res. *70*, 2264–2273.

Ekert, J.E., Johnson, K., Strake, B., Pardinas, J., Jarantow, S., Perkinson, R., and Colter, D.C. (2014). Three-dimensional lung tumor microenvironment modulates therapeutic compound responsiveness in vitro–implication for drug development. PLoS ONE *9*, e92248.

Evelyn, C.R., Duan, X., Biesiada, J., Seibel, W.L., Meller, J., and Zheng, Y. (2014). Rational design of small molecule inhibitors targeting the Ras GEF, SOS1. Chem. Biol. *21*, 1618–1628.

Fujita-Sato, S., Galeas, J., Truitt, M., Pitt, C., Urisman, A., Bandyopadhyay, S., Ruggero, D., and McCormick, F. (2015). Enhanced MET translation and signaling sustains K-Ras-driven proliferation under anchorage-independent growth conditions. Cancer Res. *75*, 2851–2862.

Giannakis, M., Mu, X.J., Shukla, S.A., Qian, Z.R., Cohen, O., Nishihara, R., Bahl, S., Cao, Y., Amin-Mansour, A., Yamauchi, M., et al. (2016). Genomic correlates of immune-cell infiltrates in colorectal carcinoma. Cell Rep. *15*, 857–865.

Hayes, T.K., Neel, N.F., Hu, C., Gautam, P., Chenard, M., Long, B., Aziz, M., Kassner, M., Bryant, K.L., Pierobon, M., et al. (2016). Long-term ERK inhibition in KRAS-mutant pancreatic cancer is associated with MYC degradation and senescence-like growth suppression. Cancer Cell *29*, 75–89.

Howes, A.L., Richardson, R.D., Finlay, D., and Vuori, K. (2014). 3-Dimensional culture systems for anti-cancer compound profiling and high-throughput screening reveal increases in EGFR inhibitor-mediated cytotoxicity compared to monolayer culture systems. PLoS ONE *9*, e108283.

Johnson, K.A. (2009). Fitting enzyme kinetic data with KinTek Global Kinetic Explorer. Methods Enzymol. *467*, 601–626.

Jordan, E.J., Kim, H.R., Arcila, M.E., Barron, D., Chakravarty, D., Gao, J., Chang, M.T., Ni, A., Kundra, R., Jonsson, P., et al. (2017). Prospective comprehensive molecular characterization of lung adenocarcinomas for efficient patient matching to approved and emerging therapies. Cancer Discov. *7*, 596–609.

Kapoor, A., Yao, W., Ying, H., Hua, S., Liewen, A., Wang, Q., Zhong, Y., Wu, C.J., Sadanandam, A., Hu, B., et al. (2014). Yap1 activation enables bypass of oncogenic Kras addiction in pancreatic cancer. Cell *158*, 185–197.

Kwong, L.N., Boland, G.M., Frederick, D.T., Helms, T.L., Akid, A.T., Miller, J.P., Jiang, S., Cooper, Z.A., Song, X., Seth, S., et al. (2015). Co-clinical assessment identifies patterns of BRAF inhibitor resistance in melanoma. J. Clin. Invest. *125*, 1459–1470.

Lamba, S., Russo, M., Sun, C., Lazzari, L., Cancelliere, C., Grernrum, W., Lieftink, C., Bernards, R., Di Nicolantonio, F., and Bardelli, A. (2014). RAF suppression synergizes with MEK inhibition in KRAS mutant cancer cells. Cell Rep. *8*, 1475–1483.

Lanning, B.R., Whitby, L.R., Dix, M.M., Douhan, J., Gilbert, A.M., Hett, E.C., Johnson, T.O., Joslyn, C., Kath, J.C., Niessen, S., et al. (2014). A road map to evaluate the proteome-wide selectivity of covalent kinase inhibitors. Nat. Chem. Biol. *10*, 760–767.

Leshchiner, E.S., Parkhitko, A., Bird, G.H., Luccarelli, J., Bellairs, J.A., Escudero, S., Opoku-Nsiah, K., Godes, M., Perrimon, N., and Walensky, L.D. (2015). Direct inhibition of oncogenic KRAS by hydrocarbon-stapled SOS1 helices. Proc. Natl. Acad. Sci. USA *112*, 1761–1766.

Li, L., Feng, J., Wu, T., Ren, P., Liu, Y., and Long, Y.O. (2015). Inhibitors of KRAS G12C. Patent WO2015054572 A1, filed October 10, 2014, and published April 16, 2015.

Liberzon, A., Birger, C., Thorvaldsdóttir, H., Ghandi, M., Mesirov, J.P., and Tamayo, P. (2015). The Molecular Signatures Database (MSigDB) hallmark gene set collection. Cell Syst. *1*, 417–425.

Lim, S.M., Westover, K.D., Ficarro, S.B., Harrison, R.A., Choi, H.G., Pacold, M.E., Carrasco, M., Hunter, J., Kim, N.D., Xie, T., et al. (2014). Therapeutic targeting of oncogenic K-Ras by a covalent catalytic site inhibitor. Angew. Chem. Int. Ed. Engl. *53*, 199–204.

Lito, P., Solomon, M., Li, L.S., Hansen, R., and Rosen, N. (2016). Allele-specific inhibitors inactivate mutant KRAS G12C by a trapping mechanism. Science *351*, 604–608.

Liu, Q., Sabnis, Y., Zhao, Z., Zhang, T., Buhrlage, S.J., Jones, L.H., and Gray, N.S. (2013). Developing irreversible inhibitors of the protein kinase cysteinome. Chem. Biol. *20*, 146–159.

MacLean, B., Tomazela, D.M., Shulman, N., Chambers, M., Finney, G.L., Frewen, B., Kern, R., Tabb, D.L., Liebler, D.C., and MacCoss, M.J. (2010). Skyline: an open source document editor for creating and analyzing targeted proteomics experiments. Bioinformatics *26*, 966–968.

Margarit, S.M., Sondermann, H., Hall, B.E., Nagar, B., Hoelz, A., Pirruccello, M., Bar-Sagi, D., and Kuriyan, J. (2003). Structural evidence for feedback activation by Ras.GTP of the Ras-specific nucleotide exchange factor SOS. Cell *112*, 685–695.

Maurer, T., Garrenton, L.S., Oh, A., Pitts, K., Anderson, D.J., Skelton, N.J., Fauber, B.P., Pan, B., Malek, S., Stokoe, D., et al. (2012). Small-molecule ligands bind to a distinct pocket in Ras and inhibit SOS-mediated nucleotide exchange activity. Proc. Natl. Acad. Sci. USA *109*, 5299–5304.

McDonald, E.R., 3rd, de Weck, A., Schlabach, M.R., Billy, E., Mavrakis, K.J., Hoffman, G.R., Belur, D., Castelletti, D., Frias, E., Gampa, K., et al. (2017). Project DRIVE: a compendium of cancer dependencies and synthetic lethal relationships uncovered by large-scale, deep RNAi screening. Cell *170*, 577–592.

Ostrem, J.M., and Shokat, K.M. (2016). Direct small-molecule inhibitors of KRAS: from structural insights to mechanism-based design. Nat. Rev. Drug Discov. *15*, 771–785.

Ostrem, J.M., Peters, U., Sos, M.L., Wells, J.A., and Shokat, K.M. (2013). K-Ras(G12C) inhibitors allosterically control GTP affinity and effector interactions. Nature *503*, 548–551.

Patgiri, A., Yadav, K.K., Arora, P.S., and Bar-Sagi, D. (2011). An orthosteric inhibitor of the Ras-Sos interaction. Nat. Chem. Biol. *7*, 585–587.

Patricelli, M.P., Janes, M.R., Li, L.S., Hansen, R., Peters, U., Kessler, L.V., Chen, Y., Kucharski, J.M., Feng, J., Ely, T., et al. (2016). Selective inhibition of oncogenic KRAS output with small molecules targeting the inactive state. Cancer Discov. *6*, 316–329.

Pickl, M., and Ries, C.H. (2009). Comparison of 3D and 2D tumor models reveals enhanced HER2 activation in 3D associated with an increased response to trastuzumab. Oncogene *28*, 461–468.

Pylayeva-Gupta, Y., Grabocka, E., and Bar-Sagi, D. (2011). RAS oncogenes: weaving a tumorigenic web. Nat. Rev. Cancer *11*, 761–774.

Selby, M., Delosh, R., Laudeman, J., Ogle, C., Reinhart, R., Silvers, T., Lawrence, S., Kinders, R., Parchment, R., Teicher, B.A., and Evans, D.M. (2017). 3D models of the NCI60 cell lines for screening oncology compounds. SLAS Discov. *22*, 473–483.

Shao, D.D., Xue, W., Krall, E.B., Bhutkar, A., Piccioni, F., Wang, X., Schinzel, A.C., Sood, S., Rosenbluh, J., Kim, J.W., et al. (2014). KRAS and YAP1 converge to regulate EMT and tumor survival. Cell *158*, 171–184.

Shima, F., Yoshikawa, Y., Matsumoto, S., and Kataoka, T. (2013). Discovery of small-molecule Ras inhibitors that display antitumor activity by interfering with Ras.GTP-effector interaction. Enzymes *34 Pt. B*, 1–23.

Singh, A., Greninger, P., Rhodes, D., Koopman, L., Violette, S., Bardeesy, N., and Settleman, J. (2009). A gene expression signature associated with "K-Ras addiction" reveals regulators of EMT and tumor cell survival. Cancer Cell *15*, 489–500.

Stepan, A.F., Walker, D.P., Bauman, J., Price, D.A., Baillie, T.A., Kalgutkar, A.S., and Aleo, M.D. (2011). Structural alert/reactive metabolite concept as applied in medicinal chemistry to mitigate the risk of idiosyncratic drug toxicity: a perspective based on the critical examination of trends in the top 200 drugs marketed in the United States. Chem. Res. Toxicol. *24*, 1345–1410.

Strelow, J.M. (2017). A perspective on the kinetics of covalent and irreversible inhibition. SLAS Discov. *22*, 3–20.

Subramanian, A., Tamayo, P., Mootha, V.K., Mukherjee, S., Ebert, B.L., Gillette, M.A., Paulovich, A., Pomeroy, S.L., Golub, T.R., Lander, E.S., and Mesirov, J.P. (2005). Gene set enrichment analysis: a knowledge-based approach for interpreting genome-wide expression profiles. Proc. Natl. Acad. Sci. USA *102*, 15545–15550.

Sun, Q., Burke, J.P., Phan, J., Burns, M.C., Olejniczak, E.T., Waterson, A.G., Lee, T., Rossanese, O.W., and Fesik, S.W. (2012). Discovery of small molecules that bind to K-Ras and inhibit Sos-mediated activation. Angew. Chem. Int. Ed. Engl. *51*, 6140–6143.

Sunaga, N., Shames, D.S., Girard, L., Peyton, M., Larsen, J.E., Imai, H., Soh, J., Sato, M., Yanagitani, N., Kaira, K., et al. (2011). Knockdown of oncogenic KRAS in non-small cell lung cancers suppresses tumor growth and sensitizes tumor cells to targeted therapy. Mol. Cancer Ther. *10*, 336–346.

Sweet-Cordero, A., Mukherjee, S., Subramanian, A., You, H., Roix, J.J., Ladd-Acosta, C., Mesirov, J., Golub, T.R., and Jacks, T. (2005). An oncogenic KRAS2 expression signature identified by cross-species gene-expression analysis. Nat. Genet. *37*, 48–55.

Vallejo, A., Perurena, N., Guruceaga, E., Mazur, P.K., Martinez-Canarias, S., Zandueta, C., Valencia, K., Arricibita, A., Gwinn, D., Sayles, L.C., et al. (2017). An integrative approach unveils FOSL1 as an oncogene vulnerability in KRAS-driven lung and pancreatic cancer. Nat. Commun. *8*, 14294.

Vartanian, S., Bentley, C., Brauer, M.J., Li, L., Shirasawa, S., Sasazuki, T., Kim, J.S., Haverty, P., Stawiski, E., Modrusan, Z., et al. (2013). Identification of mutant K-Ras-dependent phenotypes using a panel of isogenic cell lines. J. Biol. Chem. *288*, 2403–2413.

Weigelt, B., Lo, A.T., Park, C.C., Gray, J.W., and Bissell, M.J. (2010). HER2 signaling pathway activation and response of breast cancer cells to HER2-targeting agents is dependent strongly on the 3D microenvironment. Breast Cancer Res. Treat. *122*, 35–43.

Welsch, M.E., Kaplan, A., Chambers, J.M., Stokes, M.E., Bos, P.H., Zask, A., Zhang, Y., Sanchez-Martin, M., Badgley, M.A., Huang, C.S., et al. (2017). Multivalent small-molecule Pan-RAS inhibitors. Cell *168*, 878–889.

Winn, M.D., Ballard, C.C., Cowtan, K.D., Dodson, E.J., Emsley, P., Evans, P.R., Keegan, R.M., Krissinel, E.B., Leslie, A.G., McCoy, A., et al. (2011). Overview of the CCP4 suite and current developments. Acta Crystallogr. D Biol. Crystallogr. *67*, 235–242.

Xiong, Y., Lu, J., Hunter, J., Li, L., Scott, D., Choi, H.G., Lim, S.M., Manandhar, A., Gondi, S., Sim, T., et al. (2016). Covalent guanosine mimetic inhibitors of G12C KRAS. ACS Med. Chem. Lett. *8*, 61–66.

STAR★METHODS

KEY RESOURCES TABLE

REAGENT or RESOURCE	SOURCE	IDENTIFIER
Antibodies		
Rabbit monoclonal anti-RAS [EPR3255]	Abcam	Cat# ab108602; RRID: AB_10891004
Rabbit polyclonal anti-KRAS2B (C-19)	Santa Cruz Biotechnology	Cat# sc-521; RRID: AB_2134131
Rabbit monoclonal anti-phospho-ERK T202/Y204	Cell Signaling Technology	Cat# 4370; RRID: AB_2315112
Rabbit monoclonal anti-ERK	Cell Signaling Technology	Cat# 4695; RRID: AB_390779
Rabbit monoclonal anti-phospho-AKT S473 (D9E)	Cell Signaling Technology	Cat# 4060
Rabbit monoclonal anti-phospho-AKT T308 (C31E5E)	Cell Signaling Technology	Cat# 2965
Rabbit monoclonal anti-AKT	Cell Signaling Technology	Cat# 4691; RRID: AB_915783
Rabbit monoclonal anti-phospho-S6 (S235/236) (D57.2.2E)	Cell Signaling Technology	Cat# 4858
Rabbit monoclonal anti-cleaved PARP (Asp214)	Cell Signaling Technology	Cat# 9541; RRID: AB_331426
Rabbit monoclonal anti-cleaved caspase-3 (Asp175)	Cell Signaling Technology	Cat# 9664
Rabbit monoclonal anti-HSP90	Cell Signaling Technology	Cat# 4877; RRID: AB_2233307
Rabbit monoclonal anti-tubulin	Cell Signaling Technology	Cat# 2144
Rabbit monoclonal anti-FLAG (DYKDDDDK tag)	Cell Signaling Technology	Cat# 2368
Bacterial and Virus Strains		
pLenti3.3/TR from ViraPower HiPerform T-REx Gateway vector kit	ThermoFisher Scientific	A11144
pLenti6.3/TO/V5-DEST from ViraPower HiPerform T-REx Gateway vector kit	ThermoFisher Scientific	A11144
One Shot TOP10 *E. Coli*	ThermoFisher Scientific	C4040-03
One Shot BL21(DE3) *E. Coli*	ThermoFisher Scientific	C600003
Biological Samples		
Patient-derived xenografts (PDX)	CrownBio (Beijing, China)	https://www.crownbio.com/
Patient-derived xenografts (PDX)	GenenDesign (Shanghai, China)	http://genendesign.com/website/
Chemicals, Peptides, and Recombinant Proteins		
(S)-1-(4-(6-Chloro-8-fluoro-7-(2-fluoro-6-hydroxyphenyl)quinazolin-4-yl)piperazin-1-yl) prop-2-en-1-one (ARS-1620)	This paper	N/A
(R)-1-(4-(6-Chloro-8-fluoro-7-(2-fluoro-6-hydroxyphenyl)quinazolin-4-yl)piperazin-1-yl) prop-2-en-1-one (*R*-atropisomer of ARS-1620)	This paper	N/A
1-(4-(6-Chloro-8-fluoro-7-(2-fluoro-6-methoxyphenyl)quinazolin-4-yl)piperazin-1-yl) propan-1-one (ARS-1620 saturated analog)	This paper	N/A
1-(4-(6-chloro-7-phenylquinazolin-4-yl) piperazin-1-yl)prop-2-en-1-one (ARS-806)	This paper	N/A
1-(4-(6-chloro-7-(2-hydroxyphenyl)quinazolin-4-yl)piperazin-1-yl)prop-2-en-1-one (ARS-869)	This paper	N/A
1-(4-(6-chloro-7-(2-fluorophenyl)quinazolin-4-yl)piperazin-1-yl)prop-2-en-1-one (ARS-917)	This paper	N/A
1-(4-(6-chloro-7-(2-fluoro-6-methoxyphenyl) quinazolin-4-yl)piperazin-1-yl)prop-2-en-1-one (ARS-1116)	This paper	N/A

(Continued on next page)

Continued

REAGENT or RESOURCE	SOURCE	IDENTIFIER
1-(4-(6-chloro-8-fluoro-7-(2-fluorophenyl) quinazolin-4-yl)piperazin-1-yl)prop-2-en-1-one (ARS-1170)	This paper	N/A
1-(4-(6-chloro-8-fluoro-7-(2-fluoro-6-hydroxyphenyl)quinazolin-4-yl)piperazin-1-yl) prop-2-en-1-one (ARS-1323, a racemic mixture of ARS-1620/R-atropisomer)	This paper	N/A
Labrasol (as oral vehicle)	Gattefossé SAS, (Saint-Priest,France)	Cat# 3074BFE, lot# 153313
Trametinib	LC labs	Cat# T-1823
Mant-GDP	Sigma	Cat# 69244
GDP	Sigma	Cat# G7127
GTP	Sigma	Cat# G8877
Guanosine 5′-[β,γ-imido]triphosphate trisodium salt hydrate (GppNp)	Sigma	Cat# G0635
Custom heavy isotopically labeled KRAS^{G12C} 1-169 his-tagged protein (Lys-$^{13}C_6$,$^{15}N_2$ and Arg-$^{13}C_6$,$^{15}N_4$)	PROMISE Advanced Proteomics, Grenoble, France	N/A
Custom Isotopically labeled KRAS^{G12C} HeavyPeptide AQUA	ThermoFisher Scientific	N/A
Iodoacetamide desthiobiotin	This paper	N/A
Pierce High Capacity Streptavidin agarose	ThermoFisher Scientific	Cat# 20361
Critical Commercial Assays		
CellTiter-Glo Luminescent Cell Viability Assay	Promega	Cat# G7573
Active Ras Detection Kit	Cell Signaling Technology	Cat# 8821
Deposited Data		
Crystallography data	This paper	PDB: 5V9U
Transcriptome RNaseq data (fastq files and processed RPKM values)	This paper	GEO: GSE103021
Experimental Models: Cell Lines		
RAS-less mouse embryonic fibroblasts (MEFs): overexpressing KRAS 4B WT, KRAS 4B G12C, KRAS 4B G12D, and KRAS 4B G12V	NIH (NCI RAS initiative at the FNLCR) Laboratories of Rachel Bagni, Matthew Holderfield, and Dan Soppet)	N/A
293FT cell line for virus production	ThermoFisher Scientific	Cat# R70007
H358 (NCI-H358) cell line	ATCC	Cat# CRL-5807
MIA-PaCa2 cell line	ATCC	Cat# CRL-1420
SW837 cell line	ATCC	Cat# CCL-235
CALU1 cell line	ATCC	Cat# HTB-54
H23 (NCI-H23) cell line	ATCC	Cat# CRL-5800
H2122 (NCI-H2122) cell line	ATCC	Cat# CRL-5985
SW1463 cell line	ATCC	Cat# CCL-234
H2030 (NCI-H2030) cell line	ATCC	Cat# CRL-5914
H1373 (NCI-H1373) cell line	ATCC	Cat# CRL-5866
H1792 (NCI-H1792) cell line	ATCC	Cat# CRL-5895
SW1573 cell line	ATCC	Cat# CRL-2170
A549 cell line	ATCC	Cat# CCL-185
H441 (NCI-H441) cell line	ATCC	Cat# HTB-174
HCT116 cell line	ATCC	Cat# CCL-247
A375 cell line	ATCC	Cat# CRL-1619

Continued

REAGENT or RESOURCE	SOURCE	IDENTIFIER
LU65 cell line	Japanese Collection of Research Bioresources Cell Bank (JCRB)	Cat# JCRB0079
LU99A cell line	Japanese Collection of Research Bioresources Cell Bank (JCRB)	Cat# JCRB0044
HCC44 cell line	DSMZ	Cat# ACC 534
HCC1171 cell line	Korean Cell Line Bank (JCLB)	Cat# 71171
Experimental Models: Organisms/Strains		
Athymic female nude mice (NCr) nu/nu, 8-weeks old	Simonsen Labs	http://www.simlab.com/products/nudes.html
Male BALB/cAnNCrSim mice, 6- to 8-weeks old	Simonsen Labs	http://simlab.com/products.html
CD-1 mice, 6- to 8-weeks old	Charles Rivers	https://www.criver.com/products-services/basic-research/find-a-model/cd-1-mouse?loc=US
Recombinant DNA		
Truncated a.a.1-169 *KRAS* G12C;C51S; C80L;C118S for crystallography cloned into pJexpress411	DNA2.0/Shokat Lab	Ostrem et al., 2013
Truncated a.a.1-169 *KRAS* G12C in pJexpress411	DNA2.0/Shokat Lab	Ostrem et al., 2013
Truncated a.a.1-169 *KRAS* in pJexpress411	DNA2.0/Shokat Lab	Ostrem et al., 2013
Catalytic domain (594-1049) of SOS1 in ProEX HTb	Kuriyan Lab	Margarit et al., 2003
Full-length N-terminal FLAG tagged *KRAS* G12C in pLenti6.3/TO	This paper	N/A
Full-length N-terminal FLAG tagged *KRAS* G12V in pLenti6.3/TO	This paper	N/A
MISSION pLKO.1 shKRAS#1	Sigma	TRCN0000033262
MISSION pLKO.1 shKRAS#2	Sigma	TRCN0000033260
MISSION pLKO.1 luciferase shRNA control	Sigma	Cat# SHC007
Software and Algorithms		
KinTek Explorer Chemical Kinetics Software	KinTek	https://kintekcorp.com/software/
CCP4 software for crystallography	Winn et al., 2011	http://www.ccp4.ac.uk/
QIAGEN Biomedical Genomics Workbench v4.1.1	QIAGEN	https://www.qiagenbioinformatics.com/products/biomedical-genomics-workbench/
FlowJo v10.1	Flowjo	https://www.flowjo.com/solutions/flowjo
MassHunter Software	Agilent	https://www.agilent.com/en-us/products/software-informatics/masshunter-suite/masshunter/masshunter-software
Progenesis LC-MS software for proteomics V3.0	Waters	http://www.nonlinear.com/progenesis/
Proteome Discoverer software v1.4	ThermoFisher Scientific	Cat# IQLAAEGABSFAKJMAUH
Skyline Targeted Mass Spec Environment v3.6	MacLean et al., 2010	https://skyline.ms
GSEA (Java, v3.0)	Subramanian et al., 2005	http://software.broadinstitute.org/gsea/index.jsp
Project DRIVE data portal	McDonald et al., 2017	https://oncologynibr.shinyapps.io/drive/
MSigDB v6.0	Subramanian et al., 2005	http://software.broadinstitute.org/gsea/index.jsp
Prism v7.03	GraphPad Software	N/A

CONTACT FOR REAGENT AND RESOURCE SHARING

Further information and requests for resources and reagents should be directed to and will be fulfilled by the Lead Contact, Yi Liu (yi@kuraoncology.com).

EXPERIMENTAL MODEL AND SUBJECT DETAILS

Cell lines and bacterial strains

H358, MIA-PaCa2, SW837, CALU1, H23, H2122, SW1463, H2030, H1373, H1792, SW1573, A549, H441, HCT116, and A375 cells were purchased from the American Type Culture Collection (ATCC). LU65 (JCRB0079) and LU99A (JCRB0044) were purchased from the Japanese Collection of Research Bioresources Cell Bank (JCRB). HCC44 (ACC 534) was purchased from DSMZ. HCC1171 (71171) was purchased from the Korean Cell Line Bank (JCLB). Ras-less MEFs were obtained from the NIH (NCI RAS initiative at the FNLCR). All cancer cell lines at Wellspring Biosciences underwent identity validation by SNP genotyping authentication services and were tested for mycoplasma infection (IDEXX Bioresearch) before studies were conducted. All in-house cell lines within the embodied work were carried for no longer than 20 cell passages. Cells were maintained in a humidified incubator at 37°C with 5% CO_2, and grown in RPMI 1640 or DMEM supplemented with 10% FBS (GIBCO) and 50 IU ml^{-1} penicillin/streptomycin (GIBCO). *E. Coli* cells for cloning (One Shot TOP10) and protein production (One Shot BL21 Star (DE3)) were purchased from ThermoFisher Scientific. For custom heavy isotopically labeled KRAS protein standards produced at PROMISE Advanced Proteomics (Grenoble, France) the *E. Coli* strain BL21(DE3) auxotrophic for lysine and arginine (genotype: *lysA$^-$*, *argA$^-$*) was used.

Animal studies

All mouse experiments were approved by a local Animal Care and Use Committee and studies were conducted at AAALAC-accredited institutions (Explora BioLabs, CA; Crown Bioscience, Beijing, China; and GenenDesign, Shanghai, China). Mice were maintained under specific pathogen-free conditions, and food and water were provided *ad libitum*. Sample sizes were determined roughly on the basis of a power analysis using historical xenograft tumor measurement data and anti-tumor responses.

Pharmacokinetic (PK) studies in mice

For pharmacokinetic (PK) studies 6- to 8-week-old male BALB/c mice (Simonsen Laboratories, Gilroy, California) were used. To determine oral bioavailability, mice were treated with ARS-1620 by a single intravenous (IV) bolus or oral gavage administration at the doses of 2 and 10 mg/kg, respectively. ARS-1620 was formulated in water solution with 1% N-methyl-2-pyrrolidone, 19% polyethylene glycol 400, and 10% cyclodextrin and then sterilized by filtration for IV dosing. Oral formulation was prepared in solution (100% Labrasol®, Gattefossé). Drug concentration in plasma was quantified by LC-MS/MS-based methods. Pharmacokinetic parameters were estimated using Phoenix WinNonlin (version 6.3) (Certara USA, Princeton, New Jersey) from mean plasma concentration-time profiles. The area under the curve (AUC) was calculated from time versus concentration data using the linear trapezoidal rule. The oral bioavailability is calculated as the ratio of AUC for ARS-1620 from oral and IV dosage. The calculation is normalized by relative doses. In all experiments, ARS-1620 displayed greater than 50% oral bioavailability. For PK analysis from tumor samples, vials containing tumor samples were added with 5-fold water and homogenized with a bead mill homogenizer. For calibration standard or QC samples, 40 μl of blank tumor homogenate was transferred into each well of a 96-well removable tube plate and spiked with 10 μl of 5X standard stock spiking solution of ARS-1620 prepared in 100% DMSO. For PK samples, 40 μl of tumor homogenate was transferred into each well of a 96-well removable tube plate and spiked with 10 μl of 100% DMSO. All samples were added with 150 μl of 100% ice-cold acetonitrile containing internal standard and vortexed to ensure thorough mixing. Samples were centrifuged at 3,400 rpm for 10 min and the clean supernatants (30 μl) were transferred into 96-well plate containing 170 μl water with 0.1% formic acid. The plate was capped and briefly vortexed to ensure thorough mixing of the extracted samples. The samples were subjected to LC-MS/MS analysis using an Agilent Technologies 6430 Triple Quad LC/MS system.

A Phenomenex Gemini-NX column (C18, 3 μm, 110 Å, 20 mm x 2.0 mm) was used for the LC-MS/MS analysis with mobile phase A containing 10 mM NH_4HCO_3 in water (pH 10, adjusted by NH4OH) and mobile phase B containing 100% acetonitrile. The LC gradient started with 10% B at time zero till 0.3 minutes, and then was increased to 90% B at 2 minutes. The gradient was decreased from 90% B to 10% B from 2.4 minutes to 2.5 minutes, and then the column was equilibrated at 10% B till 3 minutes. The mass peak of ARS-1620 was monitored by multiple reaction monitoring (MRM) using transition of 431.1 > 124.1 amu. Chromatogram signals were integrated and calibrated using Agilent MassHunter Workstation Software B.06.00. Pharmacokinetic parameters were derived by non-compartmental analysis using Phoenix WinNonlin (version 6.3) from individual tumor concentration versus time profiles. Results are expressed as mean ± s.d. No further statistical analysis was performed.

Cell line and patient-derived xenograft studies in mice

For tumor bearing models, female 6- to 8-week-old athymic BALB/c nude (NCr) nu/nu mice were used for human cancer cell lines (Simonsen Laboratories, Gilroy, California) and patient-derived xenografts (mice from Beijing HFK Bioscience). For H358, MIA-PaCa2, H2030, HCC44, H1373, LU99A, and H441 xenografts, cells (5 × 10^6) were harvested on the day of use and injected in growth-factor-reduced Matrigel/PBS (50% final concentration in 100 μl). For the efficacy study presented in Figure 5E,

independent replication of the study was performed with comparable results (data not shown). For patient-derived xenografts, a primary human tumor model fragment (2-3 mm in diameter) was implanted for tumor development at an independent service facility (PDX-2512, −1266, −1168, - 1868, −0170 at Crown Bioscience, Beijing, China, and PDX-092, −156 at GenenDesign, Shanghai, China). Further detail regarding the identity of the human specimens used is not available. One flank was inoculated subcutaneously per mouse. Mice were monitored daily, weighed twice weekly, and caliper measurements began when tumors became visible. For efficacy studies, animals were randomly assigned to treatment groups by an algorithm that assigns animals to groups to achieve best case distributions of mean tumor size with lowest possible standard deviation. Tumor volume was calculated by measuring two perpendicular diameters using the following formula: (L x w^2) / 2 in which L and w refer to the length and width tumor diameter, respectively. Percent tumor volume change was calculated using the following formula: ($V_{final} − V_{initial}$) / $V_{initial}$ x 100. Percent of TGI was calculated using the following formula: %TGI = 100 x (1-(average $V_{final} − V_{initial}$ of treatment group) / (average $V_{final} − V_{initial}$ of control group). When tumors reached an average size of 200-400 mm^3, mice were randomized into 3-10 mice per group (n = 3 mice per group for non-G12C tumors) and treated with vehicle (100% Labrasol®, Gattefossé) or indicated compounds using a daily schedule by oral gavage. In all cases, no tumor measurement data or animals were excluded. Results are expressed as mean and standard deviation of the mean. Treatment related adverse events were not observed and no experimental procedures to reduce adverse events were used throughout the study periods described. *KRAS p.G12C* PDX models employed in this study were refractory (< 50% TGI) to standard of care treatment regimens: NSCLC models—refractory to erlotinib (50 mg/kg, p.o., qd) and cisplatin (5 mg/kg, i.p., qw) and PDX1266—refractory to gemcitabine (40 mg/kg, i.p., on days 1 and 4 per week); data not shown.

Toxicity assessment in mice

For toxicity assessment 6- to 8- week-old male and female CD-1 mice (Charles River) were administered ARS-1620 via oral gavage at doses of 0, 200, 600, and 1,000 mg/kg per day in 100% Labrasol® at 10ml/kg (n = 12 mice per group). Mortality, clinical observations, body weight, hematology, clinical chemistry, organ weights, and toxicokinetics were evaluated. No test article-related clinical observations occurred during the study. No significant drop in body weight was observed. No adverse hematological findings were found except mild increases in neutrophils at 1,000 mg/kg. No test article-related changes in clinical chemistry were noted. No test article-related changes in gross organ weights were found. Mild macroscopic inflammation in the stomach occurred at 1,000 mg/kg/day. No other indications of systemic toxicity were observed. No test article-related changes in microscopic evaluations of organs other than stomach irritation were found. At 1,000 mg/kg/day, Cmax and AUC_{0-24hr} in males and females at the end of study were 5,000-9,000 ng/ml and 35,000-131,000 ng·h/mL, respectively.

METHOD DETAILS

Chemistry and synthesis of chemical materials

Compounds, ARS-806, ARS-856, ARS-917, ARS-1116, ARS-1323, and its separated atropisomers including ARS-1620, and the saturated ARS-1620 analog synthesis are detailed separately (Data S1. Synthesis of compounds, Related to STAR Methods). Trametinib was purchased from LC Laboratories. Drugs for *in vitro* studies were dissolved in DMSO to yield 10 mM stock solutions and stored at −20°C.

All commercially available starting materials, reagents and solvents were used as supplied unless otherwise noted. Flash column chromatography was carried out on silica gel 60 (35−75 μm) eluting with ACS grade solvents. Chiral chromatographic separation of atropisomers was carried out using a CHIRALPAK AD-H column (50 × 250 mm, 5 μm) on preparative SFC-200 (Thar, Waters) instrument eluting with CO_2/methanol (50:50) at a flow rate of 130 g min^{-1}. NMR spectra were recorded on a Varian 400-MR 400 MHz spectrometer. NMR data are reported as follows: chemical shifts (δ) in ppm from an internal standard or residual solvent, multiplicity, coupling constants (J) in Hz, and integration. Analytical LC/MS was conducted on Shimadzu LCMS-2010EV using a Kinetex column (50 × 4.6 mm, 5 μ C18, 100A) with UV detection at 254 nm and an electrospray mode (ESI). The purity of the tested compounds was assessed by a Shimadzu LC/MS instrument. The purity of final compounds was determined to be ≥ 95% by HPLC.

Atropisomer interconversion

For evaluating the interconversion rate of ARS-1620, the single *S*-atropisomer was dissolved in DMSO and kept at 37°C for 3 weeks. The enantiomeric excess (e.e.) of ARS-1620 was monitored by chiral HPLC analysis at days 1, 3, 7, 14, and 21. The e.e. value remained the same (> 99%) and there was no detectable formation of the *R*-atropisomer.

Plasmids, lentiviral production, and recombinant proteins

For doxycycline induced expression of KRAS^{G12V} experiments, H358 cells were stably transduced with the tetracycline repressor-based backbone vector pLenti3.3/TR from the ViraPower HiPerform T-REx Gateway vector kit (ThermoFisher Scientific). For *KRAS* overexpression, codon-optimized cDNAs encoding N-terminal FLAG-tagged human *KRAS* (p.G12V) were cloned into pLenti6.3/TO/V5-DEST (ThermoFisher Scientific).

Amphotropic lentiviruses were produced by the co-transfection of 293FT cells with lentiviral constructs, packaging, and envelope vectors (ViraPower lentiviral expression system, ThermoFisher Scientific). At 72 hr after transfection, the cell culture medium was

filtered through a 0.45 μm filter, and the viral supernatant supplemented with 8 μg ml⁻¹ of polybrene (Sigma) was used for the infection of cells. For viral infection, 70% confluent cells in six-well dishes were infected with virus for 1 h under 600 x *g* at 37°C. Stable clones were selected using blasticidin, puromycin, or G418 (ThermoFisher Scientific).

KRAS^{G12C} and KRAS^{WT} proteins were expressed in *E. coli* as truncated (1-169), hexahistidine-tagged forms, purified, and used in biochemical studies as previously described (Ostrem et al., 2013; Patricelli et al., 2016). For SOS mediated nucleotide exchange, the catalytic domain (594-1049) of SOS1 (cloned into ProEX HTb) (Margarit et al., 2003) was expressed in *E. coli*, and purified as described (Ostrem et al., 2013).

Crystallization, data collection, and refinement

For X-ray crystallography, a truncated *KRAS* (aa1-169, with G12C; C51S; C80L; C118S mutations) construct was used. The purified protein was labeled with compound and prepared as previously described (Ostrem et al., 2013). Magnesium chloride (1 mM final) and GDP (40 μM final) were added to the freshly purified protein. After high-speed centrifugation hanging drop crystallization conditions were set up by mixing 1:1 protein and reservoir solution (29% PEG4000, 0.2 M CaCl2, 0.1 M Tris pH = 8.5). After several days at 20°C, plate-shaped crystals were observed. The crystals were cryoprotected in the crystallization solution supplemented with 15% glycerol, flash frozen and stored in liquid nitrogen prior to obtaining diffraction data at beamline 5.0.3 (100 K nitrogen stream, wavelength = 0.9765 Å) at the Berkeley Lab Advanced Light Source. Data was initially processed with iMosflm, solved by molecular replacement using Phaser and refined to the indicated statistics using Refmac (Winn et al., 2011). The refined model showed no Ramachandran outliers and 98.2% of the residues were in the favored region (Chen et al., 2010). See Table S1 for more details on data collection and refinement statistics.

KRAS biochemical modification

GDP- or GMPPNP-loaded, hexahistidine-tagged, truncated (1-169) KRAS proteins at 2 μM final concentration were incubated with 10 μM compound at RT in modification buffer (20 mM HEPES pH 7.5, 150 mM NaCl, 1 mM MgCl$_2$, and 1 mM DTT) and quenched with formic acid to 0.2% following reaction completion. The extent of covalent modification was determined by liquid chromatography, electrospray mass spectrometry analysis of the intact proteins on a Q-Exactive (ThermoFisher Scientific) mass spectrometer as previously reported (Patricelli et al., 2016). The observed rate (k_{obs}/[I]) was calculated assuming pseudo first-order reaction kinetics from the following equations:

$$\frac{d[KRASG12C]}{dt} = -k * [KRASG12C]$$

$$[KRASG12C]_t = [KRASG12C]_{t0} * e^{-kt}$$

Nucleotide exchange assay

KRAS^{G12C} protein (truncated, hexahistidine tagged) was loaded with mant-GDP (ThermoFisher Scientific) and the exchange assays with the incoming nucleotide (GDP or GTP; Sigma) were performed as previously described (Patricelli et al., 2016).

Plasma stability

Plasma stability was conducted by incubation of test compounds at the concentration of 5 μM in 2% DMSO with commercial mouse or human plasma (BioreclamationIVT, NY) at 37°C for 0, 0.5, 1, and 3 hours. After incubation the reaction was quenched with cold acetonitrile solution and centrifuged. The resulting supernatant was then analyzed by LC-MS/MS to quantify the parent compound as described above. The relative quantity of the compound at each incubation time point was expressed as percent remaining in comparison to time zero. The natural log of the percent remaining was used in the regression analysis to derive the elimination rate constant, *k*. The half-life value ($t_{1/2}$, hour) for plasma stability of the test compound was estimated according to the following equation: $t_{1/2} = Ln2/k$, where *k*, the elimination rate constant, was the negative slope of linear regression from a plot of the log of percentage compound remaining versus incubation time.

Cell proliferation assays

For comparison of anti-growth activity a CellTiter-Glo (CTG) luminescent based assay (Promega) was used. Cells (800-1,200 per well) were seeded (using the same media) in standard tissue culture-treated 96-well format plates (Corning Costar #3903) or ultra-low attachment surface 96-well format plates (Corning Costar #3474). The day after plating, cells were treated with a 9 point 3-fold dilution series of indicated compounds (100 μl final volume per well) and cell viability was monitored 5 days later according to the manufacturer's recommended instructions, where 50 μl of CellTiter-Glo reagent was added, vigorously mixed, covered, and placed on a plate shaker for 20 min to ensure complete cell lysis prior to assessment of luminescent signal.

For inducible KRAS^{G12V} rescue experiments, cells were seeded as 3D suspensions (ultra-low adherent plates) in the presence or absence of doxycycline (100 ng/ml, Sigma), 90 μl final culture media volume. 24hr later indicated concentrations of compound or

DMSO (in 10 μl) was added to the cultures. Remaining cell numbers was monitored 5 days later using the CTG assay as described above.

For experiment using Ras-less MEFs, cells were seeded as 3D suspensions (ultra-low adherent plates). The day after plating, cells were treated with a 9 point 3-fold dilution series of indicated compounds (100 μl final volume per well) and cell viability was monitored 5 days later by the CTG assay.

Cell cycle and apoptosis assays
5×10^4 cells were seeded into 24 well ULA-plates (Corning Costar #3471) and allowed to rest overnight. Cells were then treated with DMSO or indicated compounds. After 2 days of treatment, apoptosis and cell death was measured by staining with annexinV-APC (eBiosciences) and prodidium iodide (AnaSpec) or by 70% ethanol fixation followed by FxCycle Violet (ThermoFisher Scientific) staining to measure DNA content (cell cycle) and percentage of sub-diploid events by flow cytometry. Data was acquired on a MACSQuant (Miltenyi) flow cytometer and analyzed with FlowJo software V.10.1.

Lentivirus mediated shRNA knockdown
Lentiviral shRNA clones targeting luciferase (as sh-Ctrl) and *KRAS* were obtained from Sigma in the MISSION pLKO.1-puro vector with clone IDs as follows: sh*KRAS*#1: TRCN0000033262, NM_033360.2-509s1c1, sh*KRAS*#2: TRCN0000033260, NM_033360.2-407s1c1, and the luciferase shRNA control plasmid DNA (Cat# SHC007, Sigma). Lentiviruses were packaged as stated above with ViraPower lentiviral expression system (ThermoFisher Scientific).

Immunoblotting and RAS-GTP pulldown
1X Lysis buffer (25 mM Tris-HCl, pH 7.2, 150 mM NaCl, 5 mM MgCl$_2$, 5% glycerol, 1% NP40) from Active Ras Detection kit (Cell signaling Technology, #8821) was supplemented with phosphatase inhibitors (Sigma) and EDTA-free protease inhibitors (Protease inhibitor cocktail tables, Roche) and used for cell lysis. For lysates where RAS-GTP was assessed, we followed the manufacturers' recommended procedure. In brief, $0.5-1 \times 10^6$ pre-adhered cells (for 24 hr prior) were rinsed with ice-cold PBS, or if in 3D-spheroid suspensions ($0.5-1 \times 10^6$) cells (seeded in ultra-low adherent plates 24 hr prior) were pelleted at 300 x *g* for 3 min and washed with ice-cold PBS. Following this cells were lysed with 1ml (or 0.5ml) of lysis buffer containing 80 μg/ml of GST-tagged RAF-RBD for 10 min on ice. Remaining adherent cells were scraped off and lysate was centrifuged at 14,000 rpm for 5 min at 4°C. 90% of the pre-cleared lysates were subsequently added to pre-washed glutathione agarose beads for 1 hour at 4°C under constant rocking. The beads were subsequently pelleted and washed 3 times and eluted for western blotting with 40-60 μl of 1X SDS-PAGE sample buffer. The other remaining 10% of lysate was used to determine protein concentration by a Bradford protein assay (Biorad) and western blotting for indicated signaling markers.

For time course experiments extending beyond 24 hours, a minor modification to the RAS-GTP pulldown assay was made to account for significant differences in cell number and/or apoptosis induction caused by the treatment. To account for this, cell lysates were processed with half volume lysis buffer without RBD added. A small sample of lysate was saved for protein concentration determination and the rest of the lysate was snap frozen. To ensure equal amount of protein undergoes RBD pulldown; lysates were subsequently thawed (at RT) and adjusted to 1 mg/ml with lysis buffer (0.5 mL volume). Equal amounts of lysate were then added to 0.5 mL lysis buffer containing RAF-RBD (1 mL total volume). Lysates were vortexed, incubated for 10 min on ice and subsequently pre-cleared at 14,000 rpm for 5 min at 4°C. The remaining steps proceeded similar as stated above.

Proteins were separated by SDS-PAGE and transferred to nitrocellulose membranes (LifeTech) according to standard protocols. Membranes were immunoblotted with antibodies against RAS (pan-RAS antibody, EPR3255, Abcam), KRAS (isoform selective c-terminal specific KRAS antibody, C-19, Santa Cruz Biotechnology), and p-ERK$^{T202/Y204}$ (4370), ERK (4695), p-AKT^{S473} (4060), p-AKT^{T308} (2965), AKT (4691), p-S6$^{S235/6}$ (4858), cleaved PARP (9541), HSP90 (4877), tubulin (2144), and FLAG^{DYKDDDDK} tag (2368) from Cell Signaling Technology. After primary antibody incubation, membranes were probed with HRP-linked anti-rabbit IgG (1:2000) from Cell Signaling Technology and imaged using a ChemiDoc MP imaging system (Biorad).

Cysteine selectivity profiling
H358 cells (5×10^6) were treated with the indicated compounds and concentrations for 4 hours. Cells were subsequently washed and harvested for proteomic analysis by LC/MS-MS as previously described (Patricelli et al., 2016). Briefly, solvent exposed cysteines in cell lysates were labeled using 100 μM iodoacetamide desthiobiotin. Following trypsin digestion, desthiobiotinylated peptides were enriched using high-capacity streptavidin agarose (ThermoFisher Scientific). Peptide samples were analyzed using a Dionex RSLCnano LC coupled to a Q-Exactive Plus mass spectrometer (ThermoFisher Scientific). Progenesis LC-MS for proteomics v3.0 software (Waters) was used for automated run alignments, peak picking, normalization, and peak abundance calculations across the dataset. Identification of desthiobiotinylated peptides was obtained by database searching using Proteome Discoverer v1.4 (ThermoFisher Scientific). Normalized peak abundances for each peptide were exported to Excel 2013 (Microsoft). Mean values and %CV were calculated for each sample group each containing 3 biological replicates. Log$_2$ fold changes were calculated between DMSO control and treated sample groups. A two-tailed t test for each peptide was performed to determine the statistical significance between treated and DMSO control sample groups assuming equal variance.

Cellular KRAS[G12C] target engagement (G12C-TE)

Cells (30-50 x10^{3}) were treated with indicated compounds for the times listed and subsequently washed twice with PBS and prepared for protein extraction as previously described (Patricelli et al., 2016). Following iodoacetamide alkylation and trypsin digestion, the samples were analyzed by targeted LC/MS-MS analysis on a Dionex RSLCnano LC (ThermoFisher Scientific) using Skyline Targeted Mass Spec Environment v3.6 software (MacLean et al., 2010) coupled with a Q-Exactive quadrupole orbitrap mass spectrometer (ThermoFisher Scientific) as previously described (Patricelli et al., 2016). Kinetic G12C target engagement was modeled with KinTek Global Kinetic Explorer (Johnson, 2009).

Tumor KRAS[G12C] target engagement (G12C-TE)

Protein extracts from tumors were prepared in IP lysis buffer (Pierce) using a Precellys bead homogenizer. Approximately 400 μg protein was aliquoted and spiked with 1 picomole heavy isotopically labeled KRAS[G12C] 1-169 his-tagged protein (Lys-$^{13}C_6$,$^{15}N_2$ and Arg-$^{13}C_6$,$^{15}N_4$) as an internal standard. Heavy isotopically labeled KRAS[G12C] was produced in *E. coli*, with protein purity higher than 90% and an isotopic purity of more than 99% (PROMISE Advanced Proteomics, Grenoble, France). Proteins were precipitated using acetone, and re-suspended in LDS sample/reducing buffer and separated by SDS-PAGE using a 10% NuPAGE Bis-Tris gel (LifeTech), and subsequently stained with Coomassie brilliant blue (ThermoFisher Scientific). A gel band covering 15 to 25 kDa was excised from each lane, followed by in-gel trypsin digestion of the gel-embedded proteins. Released peptides from the gel were analyzed by targeted LC/MS-MS analysis on a Dionex RSLCnano LC (ThermoFisher Scientific) coupled with a Q-Exactive quadrupole-orbitrap mass spectrometer (ThermoFisher Scientific) using Skyline Targeted Mass Spec Environment v3.6 software (MacLean et al., 2010) as previously described (Patricelli et al., 2016). Briefly, precursor reaction monitoring was used to quantify the endogenous and heavy isotopic labeled tryptic KRAS[G12C] peptide LVVVGAC*GVGK [5, 15] and KRAS-NRAS normalization peptide SYGIPFIETSAK [135, 146]. Peptide light / heavy (L/H) isotope ratios were calculated from the peak areas for the endogenous and heavy isotopic labeled protein. Percent engagement was determined according to the following formula:

$$\% \; G12C - TE = 100 * \left(1 - \left(\frac{G12C^{sample}}{G12C^{Vehicle,average}} * \frac{Total\;RAS^{Vehicle,average}}{Total\;RAS^{sample}} \right) \right)$$

Immunohistochemistry (IHC)

Formalin-fixed, paraffin-embedded blocks were selected for each tumor model and 3 micron-thick tissue sections were cut for immunohistochemistry (IHC). Sections were counterstained with hematoxylin and eosin, and IHC staining following standard protocols. The following primary antibodies were used: p-ERK (4370), p-S6 (4858), p-AKT (4060), and cleaved caspase-3 (9664) from Cell Signaling Technology. Lab Vision UltraVision LP Detection system with HRP polymer was used for secondary detection (ThermoFisher Scientific). IHC scoring was performed manually under a microscope with the following criteria by a blinded investigator at Crown Bioscience (Beijing): 0 (negative), 1 (weak staining), 2 (medium staining), and 3 (strong staining).

Transcriptome sequencing, library preparation, and gene set analysis

RNA was extracted from cells using the QIAGEN RNeasy mini kit. RNA library preparations, sequencing reactions were conducted at GENEWIZ, Inc (South Plainfield, NJ). The NEBNext Ultra RNA library Prep kit (New England BioLabs) was used for RNA library preparation. In brief, poly(A) mRNA was enriched with oligo d(T) beads and fragmented (15 min at 94°C). cDNA fragments was subsequently synthesized, end repaired and adenylated at 3′ends, followed by universal adaptor ligation, index addition, and library enrichment with limited cycle PCR. Pooled RNA libraries were sequenced using the Illumina HiSeq 2500 system in High Output 2x150 paired-end configuration generating on average 20 million reads per biologic replicate. Data analysis was performed with the Biomedical Genomics Workbench version 3.0.0 (QIAGEN) using default settings. Sequence reads were mapped to the human reference genome (build GRCh37/hg19) using default mode of the EM estimation algorithm employed. Data were normalized using TMM (weighted trimmed mean of M-values) and implemented for differential gene expression using a negative binomial model as implemented with EdgeR within the Advanced RNaseq analysis tools package of the Biomedical Genomics Workbench. For downstream analysis normalized data were converted to RPKM and log$_2$ transformed. Genes without at least 2 reads were excluded from further analysis. Clusters presented are visualized by the Euclidean distance with average linkage. Gene sets representing ERK signatures and curated KRAS dependency genes were obtained from previous reports (Bild et al., 2006; Chiaradonna et al., 2006; Dry et al., 2010; Kwong et al., 2015; Liberzon et al., 2015; Singh et al., 2009; Sweet-Cordero et al., 2005; Vallejo et al., 2017). Enrichment of the obtained gene sets was analyzed with GSEA v3.0 (Subramanian et al., 2005). To identify enriched gene sets, we queried the MSigDB gene set database for Hv6.0 collection of hallmark sets, C2v6.0 collection of chemical and genetic pertubations (CGP) and canonical pathways (CP), C5v6.0 collection of GO biological and molecular function, and C6v6.0 collection of oncogenic signatures using separate GSEA runs with 1,000 permutations (gene set), classic p = 0 enrichment statistic, with default ranking parameters.

Targeted sequencing and library preparation

DNA was extracted from early-passage patient-derived tumor grafts, normal human blood samples (n = 3 pooled), and from normal blood of the same mouse strain as those used to grow the xenografts using the QIAGEN DNA blood mini kit. Genomic DNA was

fragmented by acoustic shearing, adaptor-ligated, fractionated and amplified for Illumina TruSeq library construction (Illumina) according to the manufacturer's instructions at GENEWIZ, Inc (South Plainfield, NJ). Targeted exonic (229 cancer-related genes) and intronic regions (13 cancer-related genes) were captured using a custom targeted panel (SureSelect^{XT}, Agilent) according to the manufacturer's instructions. Hybrid-captured DNA fragments were amplified, and subsequently indexed with Illumina primers following the manufacturer's instructions. The pooled libraries were sequenced using Illumina HiSeq2500 instrumentation (Illumina) with a 100-bp paired-end rapid run configuration.

Data analysis was performed with the Biomedical Genomics Workbench version 3.0.0 (QIAGEN) using default settings. Sequence reads were trimmed and aligned to the human reference genome (build GRCh37/hg19) using default mode, and BAM files were indel realigned and base quality scores were recalibrated. Duplicate and non-target reads were omitted from variant calling and the resulting coverage was calculated from remaining on-target reads. Mean tumor and mean normal tissue coverage was > 500X. Low frequency variant detection tool was used for variant calling with VAF less than 5% discarded. Raw variants were filtered against the reference mouse genome (mm10) to remove mouse-specific variants and from the dbSNP138, 1000 Genomes project, and HapMap databases for commonly occurring SNPs. Variants called from pooled normal human donors and mouse host samples were additionally filtered. Disease associated variants annotated in the ClinVar and COSMIC databases were retained. Finally, mutations were filtered to exclude silent changes, while retaining mutations resulting in missense, nonsense, and frameshift alterations. A manual visual inspection step was used to further remove artifactual changes. The main text reports a subset of observed variants for each model (*KRAS*, *EGFR*, and *TP53*) that was present in at least 50% of the read pairs in the tumor graft sample. See Table S4 for additional variant calls of *KRAS p.G12C* mutant PDX samples.

QUANTIFICATION AND STATISTICAL ANALYSIS

No statistical methods were used to predetermine sample size. Analyses were conducted with GraphPad Prism version 7.03 for Windows (GraphPad Software, La Jolla, CA. USA). All reported *P value*s are two-tailed, and for all analyses, p $\leq$ 0.05 is considered statistically significant, unless otherwise specified. For descriptive statistics, the group means $\pm$ s.d. was presented for all relevant data figures. The unpaired t test was used for comparisons between two-group means, under the assumption of normality. ANOVA was used for comparison of means between > 3 groups under the assumption of normality with Tukey's or Dunnet's post hoc test applied to account for multiple comparisons. The non-parametric Mann-Whitney test was used to compare the mean ranks between two groups. The non-parametric Kruskal-Wallis test was used for comparison of means between > 3 groups with Dunn's post hoc comparison to account for multiple comparisons. Tukey box and whiskers plots indicate median and interquartile range (IQR).

DATA AND SOFTWARE AVAILABILITY

The experiments and investigators, unless mentioned, were not blinded to allocation during outcome assessment. Investigators (Crown Bioscience, Beijing) that conducted the *in vivo* PDX and IHC studies were shipped vehicle and ARS-1620 and blinded to the compound attributes. For IHC studies, the images were scored by a blinded investigator at Crown Bioscience (Beijing). Raw data was compiled, processed, and annotated as described at Wellspring Biosciences. The accession number for the crystal structure coordinates reported in this paper is PDB: 5V9U. Raw (Fastq files) and processed RNaseq (RPKM values) data is publicly available through GEO: GSE103021. Raw and processed targeted NGS data from patient-derived tumor samples is available from the corresponding author upon request.
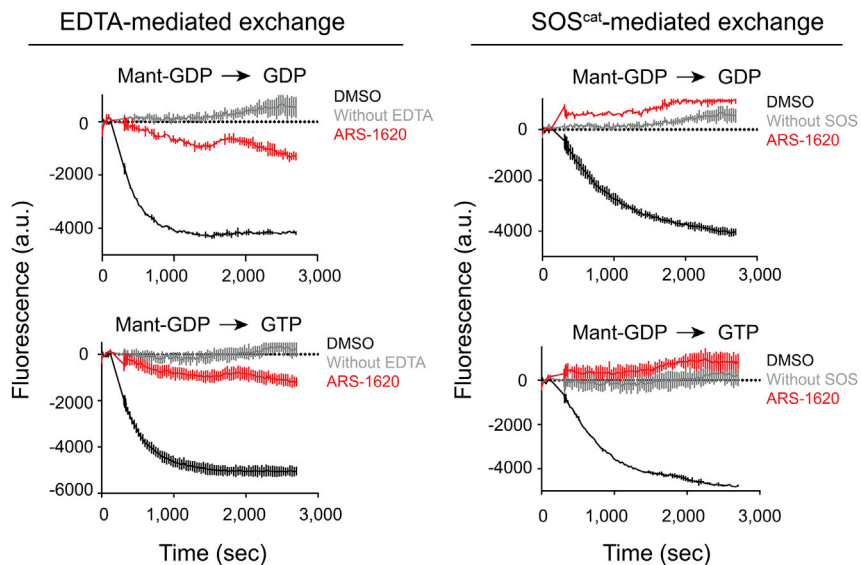
Figure S1. Functional Biochemical Effects of ARS-1620 on Blocking Nucleotide Exchange, Related to Figure 2F

Mant-GDP bound KRAS[G12C] protein pre-labeled with ARS-1620 underwent nucleotide exchange mediated by either a recombinant catalytic subunit of SOS1 (SOS[cat]) or EDTA, with unlabeled GDP (top panel) or GTP (bottom panel) as excess incoming nucleotide.
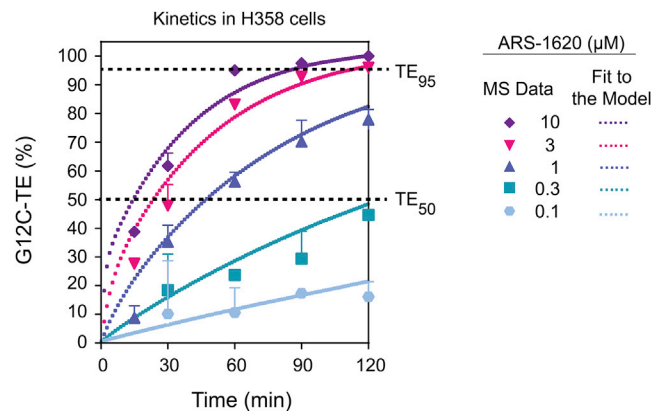
Figure S2. Fit of ARS-1620 Cellular G12C Engagement to Kinetic Model, Related to Figure 2E

LC/MS-MS analysis of KRAS[G12C] engagement (G12C-TE) following treatment of H358 cells with ARS-1620 overlaid with a fit (dotted lines) based on nonlinear regression to a kinetic model prediction. Data are represented as mean ± s.d, from n = 3 technical replicates per data point. The kinetic model incorporates parameters for baseline GDP/GTP-bound KRAS[G12C] and nucleotide cycling as described (Patricelli et al., 2016) with ARS-1620 rates reported in Figure 2E with best-fit values to the experimental data.
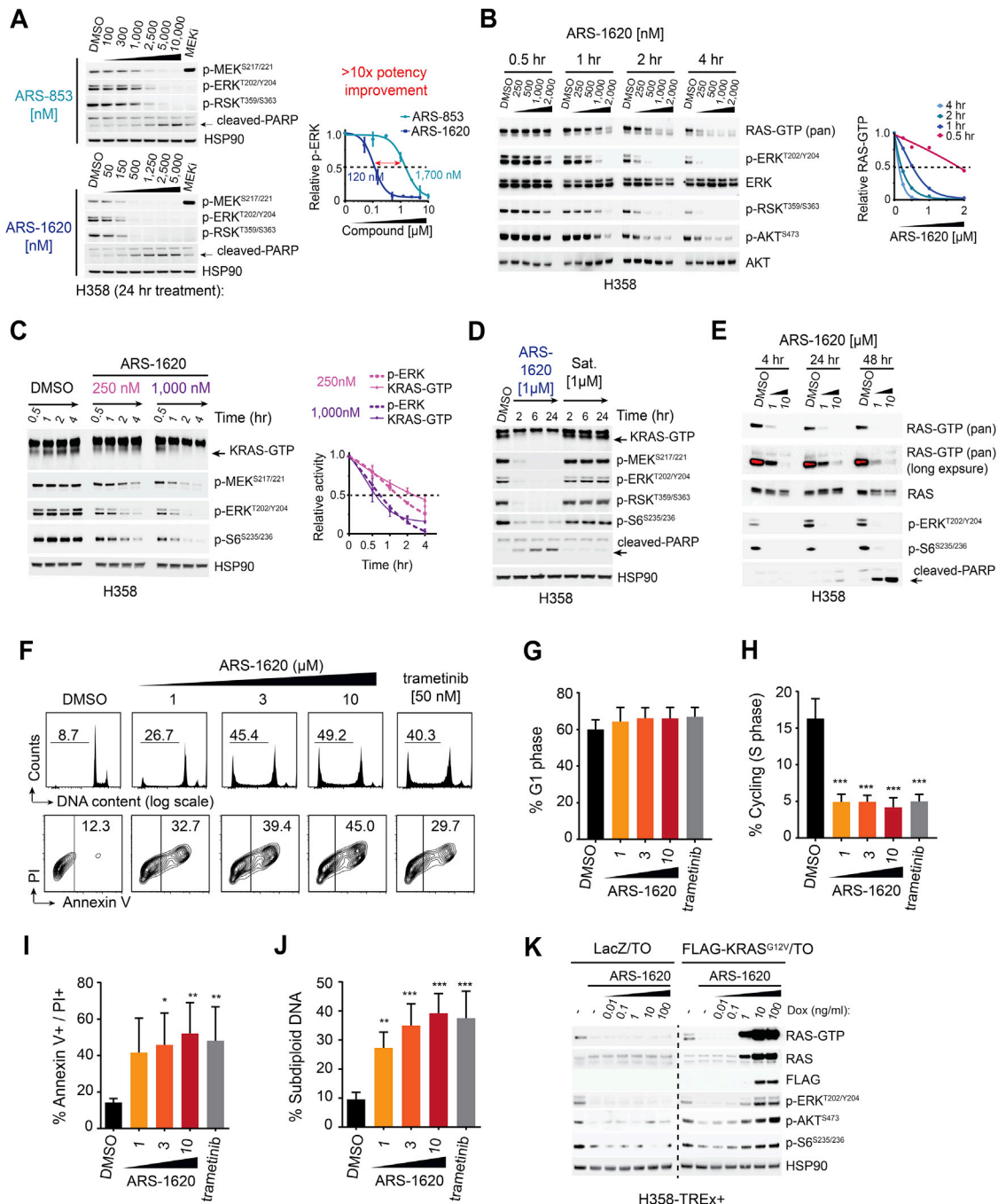
Figure S3. Improved Potency and Kinetics of ARS-1620 on Inhibiting KRAS[G12C] Signaling Compared to ARS-853 Series, Related to Figure 3

(A) Dose response of H358 cells treated with ARS-853 or ARS-1620 for 24 hr and assessed by immunoblotting. Right panel depicts normalized quantitation of p-ERK signal relative to DMSO treatment from n = 2 independent experiments.

(B and C) Immunoblot analysis of H358 cells treated over a time course and increasing concentrations of ARS-1620 (left panel). Normalized quantitation of relative RAS-GTP, KRAS-GTP, or p-ERK was compared to DMSO treated samples. (B) Pan-isoform selective anti-RAS antibody (EPR3255) was used to detect RAS-GTP from RBD-pulldown fraction (left panel) and relative quantitation (right panel).

(C) C terminus isoform selective anti-KRAS antibody (C-19; sc-521) was used detect KRAS-GTP from RBD-pulldown fraction (left panel) and relative quantitation (right panel, n = 2 independent experiments).

(D) Immunoblot of H358 cells treated over a time course of ARS-1620 (1μM) or a saturated analog of ARS-1620 (1μM). C terminus isoform selective anti-KRAS antibody (C-19; sc-521) was used to detect KRAS-GTP from RBD-pulldown fraction.

(legend continued on next page)

(E) Immunoblot of H358 cells treated over a time course and dose response of ARS-1620 (1 and 10 μM). Pan-isoform selective anti-RAS antibody (EPR3255) was used to detect RAS-GTP from RBD-pulldown fraction.

(F–J) Cell lines (n = 5, H358, H2030, H1373, HCC44, H1792) treated with ARS-1620 (μM) or trametinib (50 nM) for 48 hr and harvested for cell cycle and apoptosis analysis by flow cytometry. $*p < 0.05$, $** p < 0.01$, $***p < 0.001$. (F) Representative cell cycle analysis and apoptosis induction of H358 cells. (G) Percentage of cells in G1 phase. (H) Percentage of cells cycling in S phase. (I) Percentage of apoptosis by annexin V and PI staining. (J) Percentage of apoptosis by sub-diploid DNA content.

(K) H358 cells inducibly overexpressing LacZ or FLAG-KRAS^{G12V} were cultured with or without indicated concentrations of doxycycline for 24 hr and subsequently treated with ARS-1620 (1 μM) for 4 hr and harvested for RAS-GTP pulldown and immunoblotting. Pan-isoform selective anti-RAS antibody (EPR3255) was used to detect RAS-GTP from RBD-pulldown fraction.
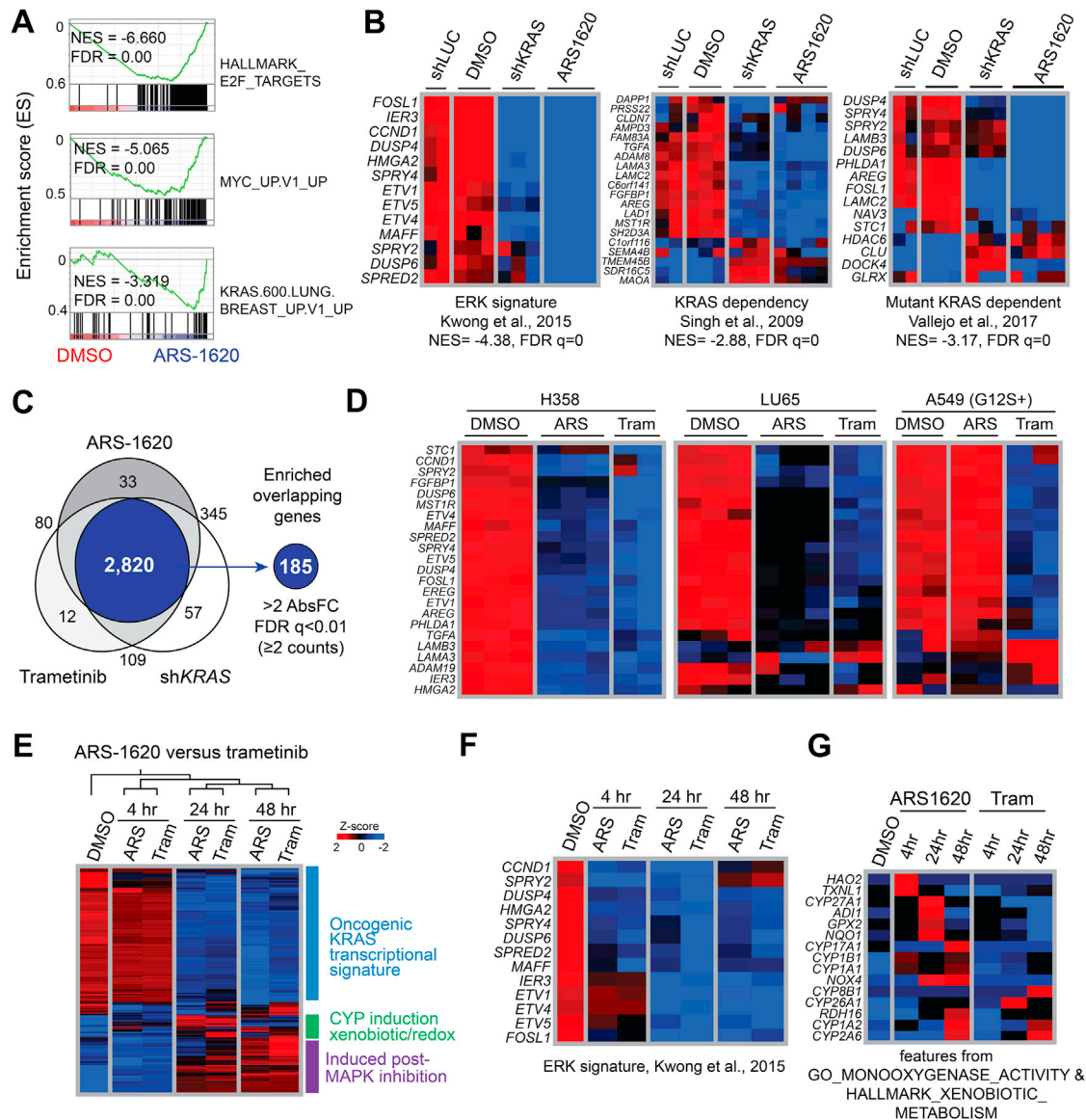
Figure S4. Gene Transcription Signatures of ARS-1620 Overlap with RAS Pathway Inhibition, Related to Figures 4C and 4D and Tables S2 and S3

(A) GSEA plots showing representative gene sets with negative enrichment following ARS-1620 treatment (1μM) or *KRAS* knockdown in H358 cells, related to Figures 4C and 4D.

(B) Heatmaps of gene sets associated with ERK activity (left) or mutant KRAS dependency (middle and right) that are negatively enriched following ARS-1620 treatment or *KRAS* knockdown, related to Figures 4C and 4D. Below each map are normalized enrichment scores (NES) for ARS-1620 regulated genes. See Table S2 for a full list of GSEA results.

(C) Venn diagram illustrating overlap of differentially expressed genes (FDR < 0.01) following ARS-1620 treatment, trametinib treatment, or *KRAS* knockdown. See Table S3 for a list of enriched genes with significant overlap and > 2 log$_2$ absolute fold change.

(D) Hierarchical clustering of a customized gene set composed of curated mutant KRAS dependency genes and ERK transcriptional targets. Differential expression was determined by comparing H358 and LU65 (*p.G12C*) or A549 (*p.G12S*) KRAS mutant lung cancer cell lines treated with ARS-1620 (ARS, 1 μM, 3 biologic replicates) or trametinib (Tram, 50 nM, 2 biologic replicates) for 24 hr.

(E) Unsupervised hierarchical clustering of top 300 differentially expressed genes following a time course treatment with ARS-1620 (ARS, 1 μM) or trametinib (Tram, 50 nM) in H358 cells.

(F) Heatmap of ERK transcriptional targets.

(G) Heatmap of genes positively enriched in GO biologic function for monooxygenase and xenobiotic metabolism (ex. P450).
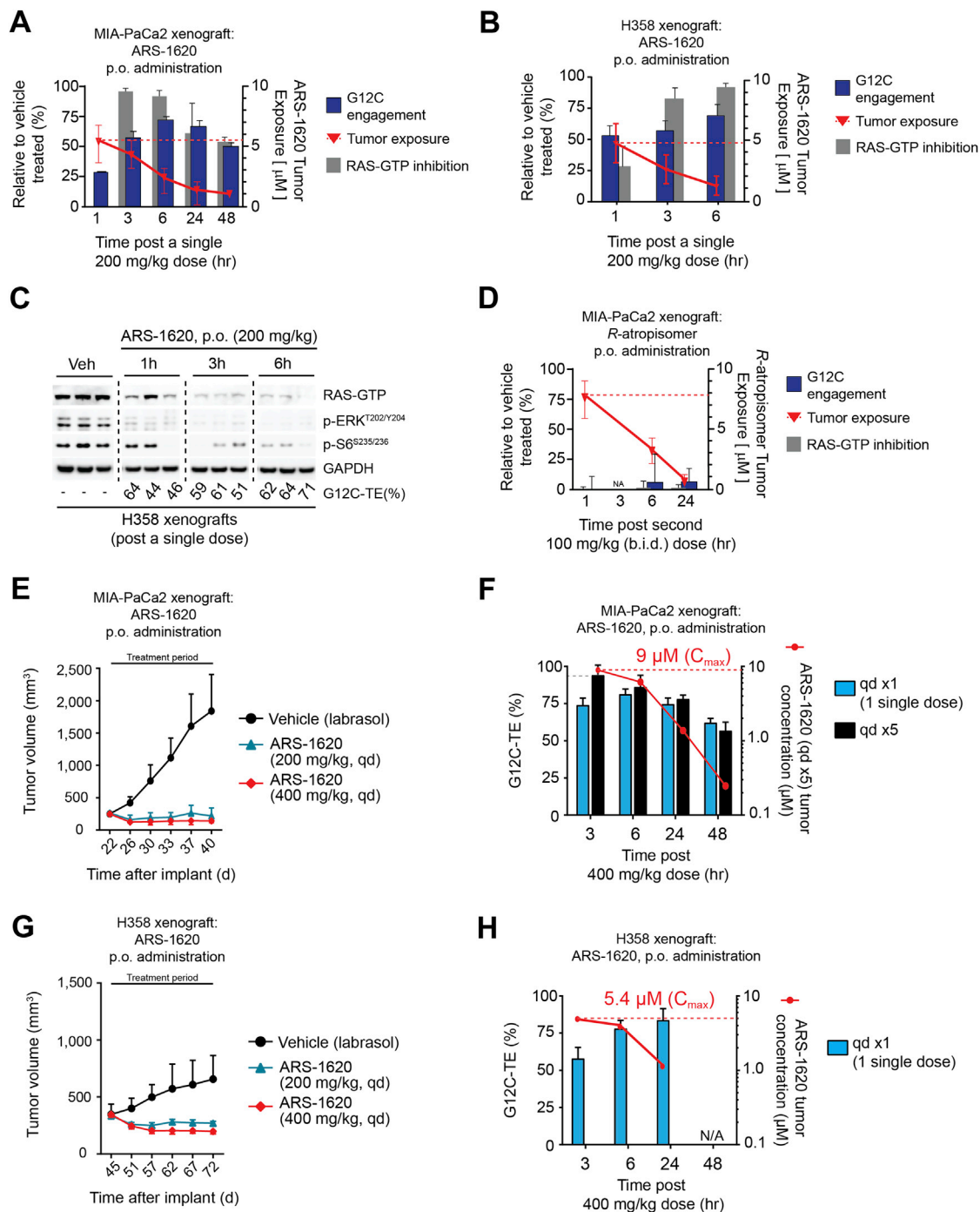
Figure S5. Pharmacokinetic Assessment of ARS-1620 and *R*-Atropisomer in Tumor-Bearing Mice, Related to Figure 5

(A) Quantitation of G12C engagement, RAS-GTP inhibition, and concentration of ARS-1620 (μM) in tumors following a single oral dose of ARS-1620 (200 mg/ kg) to subcutaneous MIA-PaCa2 xenografts. Presented as group mean ± s.d., n = 3 per time point.

(B) Quantitation of G12C-TE, RAS-GTP inhibition, and concentration of ARS-1620 (μM) in tumors following a single oral dose of ARS-1620 (200 mg/kg) to subcutaneous H358 xenografts. Tumors harvested at indicated times (hr) after treatment. Presented as group mean ± s.d., n = 3 per time point.

(C) Immunoblot, RAS-GTP pulldown, and quantitation of G12C-TE of H358 tumors following a single oral dose of 200 mg/kg of ARS-1620 at the indicated times. Pan-isoform selective anti-RAS antibody was used to detect RAS-GTP from RBD-pulldown fraction.

(D) Quantitation of G12C-TE and concentration of *R*-atropisomer (μM) in tumors following the second oral dose of 100 mg/kg b.i.d. spaced 12 hours apart.

(E) Anti-tumor efficacy of ARS-1620 in subcutaneous MIA-PaCa2 xenografts comparing daily 200 mg/kg versus 400 mg/kg treatment schedules (n = 8 per group).

(legend continued on next page)

(F) PK/PD assessment of G12C-TE and concentration of ARS-1620 (μM) in tumors following a single (qd x1) or five consecutive days (qd x5) of oral administration to MIA-PaCa2 xenografts at 400 mg/kg (n = 3 per group).

(G) Anti-tumor efficacy of ARS-1620 in subcutaneous H358 xenografts comparing daily 200 mg/kg versus 400 mg/kg treatment schedules (n = 8 per group).

(H) PK/PD assessment of G12C-TE and concentration of ARS-1620 (μM) in tumors following a single oral administration to H358 xenografts at 400 mg/kg (n = 3 per group).
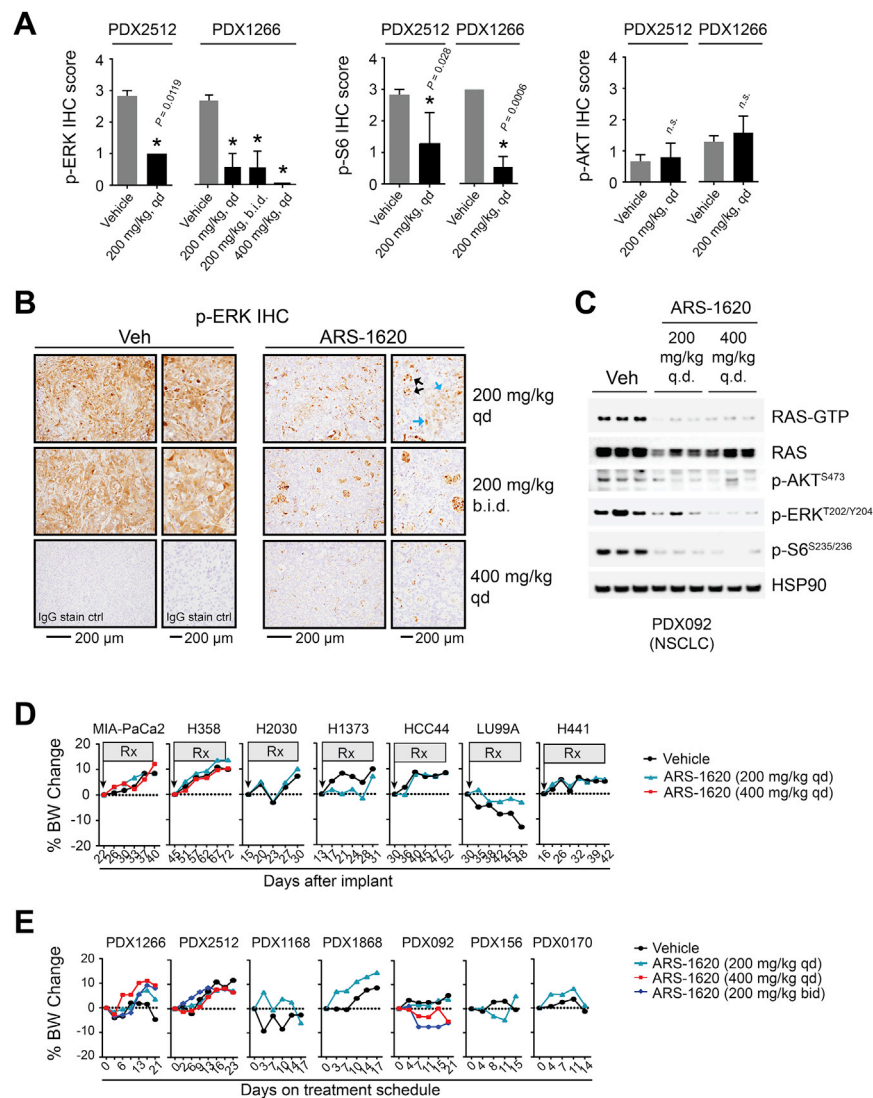
Figure S6. RAS Signaling Inhibition in *KRAS p.G12C* Mutant PDX Models, Related to Figures 6 and 7

(A) Quantitation of IHC scores from indicated PDX tumors (n = 3-7 per group, unpaired two-tailed Mann-Whitney test) for phospho-ERK (T202/Y204), phospho-S6 (S235/236), and phospho-AKT (S473).

(B) IHC assessment of p-ERK from representative PDX1266 tumors following 3 wks of treatment (1 hr after last dose). Black arrows indicate background non-specific staining, and blue arrows indicate representative positive staining. Negative control IgG staining is depicted in lower left panel.

(C) Immunoblot analysis of RAS-GTP and downstream signaling inhibition of PDX092 treated with ARS-1620 for 3 weeks (6hr after last dose).

(D and E) Mice were administered compounds daily by oral gavage starting at the indicated day after implant or when tumors were on average 200 mm^3. Data are presented as group mean (n = 3-10 mice per group). (D) Percent change in body weight of nude mice bearing subcutaneous cell-derived xenografts. (E) Percent change in body weight of nude mice bearing PDX subcutaneous xenografts.